Materials Today Bio 20 (2023) 100666

Contents lists available at ScienceDirect

Materials Today Bio

journal homepage: www.journals.elsevier.com/materials-today-bio

3D-printed placental-derived bioinks for skin tissue regeneration with improved angiogenesis and wound healing properties

Zahra Bashiri [a,b,1], Motahareh Rajabi Fomeshi [c,d,1], Hatef Ghasemi Hamidabadi [e,f], Davod Jafari [g], Sanaz Alizadeh [c,d], Maryam Nazm Bojnordi [e,f], Gorka Orive [h,i,j,k,l], Alireza Dolatshahi-Pirouz [m], Maria Zahiri [n,o,**], Rui L Reis [p], Subhas C Kundu [p], Mazaher Gholipourmalekabadi [c,g,d,*]

[a] Department of Anatomy, School of Medicine, Iran University of Medical Sciences, Tehran, Iran
[b] Omid Fertility & Infertility Clinic, Hamedan, Iran
[c] Cellular and Molecular Research Centre, Iran University of Medical Sciences, Tehran, Iran
[d] Department of Tissue Engineering & Regenerative Medicine, Faculty of Advanced Technologies in Medicine, Iran University of Medical Sciences, Tehran, Iran
[e] Department of Anatomy & Cell Biology, Faculty of Medicine, Mazandaran University of Medical Sciences, Sari, Iran
[f] Immunogenetic Research Center, Department of Anatomy & Cell Biology, Faculty of Medicine, Mazandaran University of Medical Sciences, Sari, Iran
[g] Department of Medical Biotechnology, Faculty of Allied Medicine, Iran University of Medical Sciences, Tehran, Iran
[h] NanoBioCel Research Group, School of Pharmacy, University of the Basque Country (UPV/EHU), 01006, Vitoria-Gasteiz, Spain
[i] Bioaraba, NanoBioCel Research Group, 01009, Vitoria-Gasteiz, Spain
[j] Biomedical Research Networking Centre in Bioengineering, Biomaterials and Nanomedicine (CIBER-BBN), Institute of Health Carlos III, Av Monforte de Lemos 3-5, 28029, Madrid, Spain
[k] University Institute for Regenerative Medicine and Oral Implantology-UIRMI (UPV/EHU-Fundación Eduardo Anitua), 01007, Vitoria-Gasteiz, Spain
[l] Singapore Eye Research Institute, The Academia, 20 College Road, Discovery Tower, Singapore, 169856, Singapore
[m] Department of Health Technology, Technical University of Denmark, 2800 Kgs, Lyngby, Denmark
[n] The Persian Gulf Marine Biotechnology Research Center, The Persian Gulf Biomedical Sciences Research Institute, Bushehr University of Medical Sciences, Bushehr, Iran
[o] Department of Anatomical Sciences, School of Medical Sciences, Bushehr University of Medical Sciences, Bushehr, Iran
[p] 3Bs Research Group, I3Bs - Research Institute on Biomaterials, Biodegradable and Biomimetics, Headquarters of the European Institute of Excellence on Tissue Engineering and Regenerative Medicine, University of Minho, AvePark, Guimaraes, Portugal

ARTICLE INFO

Keywords:
Placenta
Extracellular matrix
ECM bioink
Alginate/gelatin
3D printed scaffold
Wound healing

ABSTRACT

Extracellular matrix (ECM)-based bioinks has attracted much attention in recent years for 3D printing of native-like tissue constructs. Due to organ unavailability, human placental ECM can be an alternative source for the construction of 3D print composite scaffolds for the treatment of deep wounds. In this study, we use different concentrations (1.5%, 3% and 5%w/v) of ECM derived from the placenta, sodium-alginate and gelatin to prepare a printable bioink biomimicking natural skin. The printed hydrogels' morphology, physical structure, mechanical behavior, biocompatibility, and angiogenic property are investigated. The optimized ECM (5%w/v) 3D printed scaffold is applied on full-thickness wounds created in a mouse model. Due to their unique native-like structure, the ECM-based scaffolds provide a non-cytotoxic microenvironment for cell adhesion, infiltration, angiogenesis, and proliferation. In contrast, they do not show any sign of immune response to the host. Notably, the biodegradation, swelling rate, mechanical property, cell adhesion and angiogenesis properties increase with the increase of ECM concentrations in the construct. The ECM 3D printed scaffold implanted into deep wounds increases granulation tissue formation, angiogenesis, and re-epithelialization due to the presence of ECM components in the construct, when compared with printed scaffold with no ECM and no treatment wound. Overall, our findings

* Corresponding author. Department of Medical Biotechnology, Faculty of Allied Medicine, Iran University of Medical Sciences, Tehran, 1449614535, Iran.
** Corresponding author. The Persian Gulf Marine Biotechnology Research Center, The Persian Gulf Biomedical Sciences Research Institute, Bushehr University of Medical Sciences, Bushehr, Iran.
E-mail addresses: maria_zahiri@yahoo.com (M. Zahiri), mazaher.gholipour@gmail.com, mazaher.gholipour@iums.ac.ir (M. Gholipourmalekabadi).
[1] Equally contributed to this study.

https://doi.org/10.1016/j.mtbio.2023.100666
Received 11 December 2022; Received in revised form 29 April 2023; Accepted 12 May 2023
Available online 20 May 2023
2590-0064/© 2023 The Authors. Published by Elsevier Ltd. This is an open access article under the CC BY-NC-ND license (http://creativecommons.org/licenses/by-nc-nd/4.0/).

demonstrate that the 5% ECM 3D scaffold supports the best deep wound regeneration *in vivo*, produces a skin replacement with a cellular structure comparable to native skin.

1. Introduction

Over the years, engineered skin replacements have been used as a new tool to treat deep wounds. Along these lines, the main challenge has always been to restore the angiogenic potential that is severely affected in deep wounds [1–10]. As we speak, no skin alternatives in the market can promote collagen production, cell proliferation, and especially angiogenesis while reducing infection. This intimately linked with the fact that synthetic materials do not have the cellular recognition signals that connect the cell to the extracellular matrix (ECM). Natural biomaterials, including native tissue-derived ECM, are biocompatible and applicable for making scaffolds or living tissue structures. Collagen, the main protein of the ECM, is considered a natural substance for skin replacement, but it is mechanically weak and is, therefore, easily destroyed during transplantation [11–14]. To date, skin scaffolds in various forms, such as hydrogel, fiber, film, sponge, and (three dimensional)3D-printed scaffolds, have been introduced to manage different skin injuries. Among them, 3D printing scaffolds have some advantages, such as precise, well-defined and controlled 3D structures that make them excellent candidates for the engineering and fabrication of precise tissue engineering scaffolds [15]. 3D printing is a technique for creating functional organs or structures that allows cells to accumulate and mature in functional tissues [15–17]. They do that through their ability to produce well-defined 3D structures with controlled shapes and pores [18]. This approach relies primarily on hydrogels as bio-ink [19], as hydrogels in many ways resemble the native environment of tissues. This, in turn, also makes them conducive to cell growth and survival and thus makes them excellent candidates for tissue engineering. Mainly, shear-thinning hydrogels are extensively employed in 3D printing because of their capacity to deliver scaffolds with controlled shape, size, and porosity. The biomaterials used to produce printed scaffolds are frequently based on synthetic or natural polymers [20]. Several synthetic materials have been 3D printed for different applications in tissue engineering. However, a biological-based 3D printed platform alone or in combination with other synthetic or natural biomaterials proven more effective in biomimicking normal tissue composition and structure [21–24]. Indeed, several studies have shown that ECM components can lead with the aid of host cells to vascular regeneration and matrix recovery [25,26]. In summary, studies have shown that ECM-based scaffolds offer excellent substrates for maintaining important cellular functions, including migration, proliferation and differentiation. Some of them can also minimize scar formation and immune responses [27–29]. In this regard, decellularization to eliminate host cells with minimal damage to the ECM contents reduces the risk of transplant rejection [30–32].

In this direction, the decellularized ECM can be dissolved to form a hydrogel and used as a biological compound to produce an artificial structure that offers an optimal environment for cell growth [33–35]. 3D printing of ECM is very challenging because of its weak mechanical property. Consequently, a printable structure made of solid materials is required [33]. Some ECM bio-inks have been investigated for diverse tissues, such as adipose, cartilage, testis, and heart tissue, with great cellular function and survival [36–39]. In this study, we aimed to circumvent these challenges by creating a bioink from shear-thinning sodium alginate and gelatine containing different placental ECM concentrations. The shear-thinning capacity of sodium alginate gives it a high extrusion ability and subsequent stabilization of the printed system [40]. At the same time, gelatin, through it's positive amino groups, can easily bind to the negatively charged sodium backbone. It simultaneously gives rise to good cell adhesion properties through it's cell adhesive RGD sequence [41,42].

The placenta is an organ excreted after birth, and it is a rich source of ECM [43] providing a wide range of growth factors and cytokines, including epidermal growth factor (EGF), transforming growth factor (TGF), fibroblast growth factor (FGF), platelet-derived growth factor (PDGF), endothelial growth factor, and vascular endothelial growth factor (VEGF) [44]. These growth factors are all pivotal in securing optimal skin, angiogenesis and wound regeneration. One of the advantages of using placental tissue is the easy availability of a large volume of tissue after parturition and the lack of the need for an invasive procedure to obtain tissue [45]. Indeed, as a result of growth factors and filaments, including collagen, laminin, and elastin, placental ECM is an excellent option for designing and building a functional skin-like structure that can be utilized to transplant and repair wounds. In this study, a bioink was prepared and optimized using different concentrations of solubilized placental tissue, sodium alginate and gelatin. The biomechanical and biological properties of the 3D-printed scaffolds were fully characterized. The optimized ECM-based 3D-printed scaffold was applied to a deep wound created in the mouse model, and its potential in angiogenesis and wound healing was studied *in vivo*.

2. Materials and methods

2.1. Preparation and decellularization of human placental tissue

The human placenta was collected and decellularized by a procedure described in detail in our previously published studies [46,47]. In brief, the placental tissue of healthy mothers without sexually transmitted diseases, syphilis, hepatitis B, C, and AIDS, was prepared by presenting a consent form and transferred to the lab in an ice-filled standard saline solution with the antibiotic gentamicin. Placenta tissue was cut into small pieces. After washing with distilled water, placental tissue fragments were decellularized using 0.3% and 0.5% sodium dodecyl sulfate (SDS, USA, SDS, Sigma-Aldrich) and Triton X-100 (T), respectively. The decellularization process was continued by washing the samples with phosphate-buffered saline (PBS) for one week. The PBS solution was refreshed ten times to eliminate detergents and cell debris.

2.2. Decellularization characterizations

The samples were stained with hematoxylin-eosin (H&E) and 4′,6-diamidino-2-phenylindole (DAPI; Thermo Scientific), and the presence of nucleated cells was compared with the control sample to demonstrate tissue decellularization. In brief, the tissues before and after decellularization were fixed with 10% formalin, dehydrated through a graded ethanol series, and embedded in paraffin. The samples in paraffin blocks were sectioned and stained with H&E and DAPI. The H&E-stained sections were assessed under a light microscope (Olympus, Japan) using an Olympus DP72 digital camera. Fluorescence microscopy was used to observe the DAPI-stained cells (Olympus, Japan). The total DNA of the tissues before and after decellularization was extracted using a QiaAmp mini kit (Qiagen, USA). The NanoDrop spectrophotometer was used to quantify the DNA content (2000C, Thermo Fisher Scientific, USA). Further characterizations of the decellularized placenta are presented in our previous studies [46,47].

2.3. Solubilization of decellularized human placenta

The solubilization of the decellularized human placenta was carried out by our previously published protocol [48]. Briefly, the resulting plate in the previous step was homogenized in 100 ml of 4 M urea buffer (240 g urea, 6 g Tris, and 9 g NaCl in 1 L of distilled water) on a magnetized

stirrer for 24 h and then centrifuged at 14,000 rpm for 20 min. The supernatant was transferred to a dialysis bag and placed in 1 L of TBS solution (6 g of TBS Tris and 9 g of NaCl in 1 L of distilled water) and 2.5 ml of chloroform for sterilization. The dialysis bag's contents were centrifuged at 3000 rpm for 15 min to eliminate the polymerized proteins. The supernatant (viscous matrix) was collected and stored at −80 °C. ECM was frozen at −80 °C, dried under vacuum (Alpha 1–2 LD plus, Christ, Germany) overnight, and stored at −20 °C until use. The minimal effects of solubilization on collagen content of the placenta was confirmed in our previous study [48].

2.4. Fabrication of placenta ECM-loaded alginate/gelatin 3D print scaffolds

2.4.1. Preparation of ECM solution for pre-gel

The ECM solution was made by adding various concentrations of ECM powder (1.5, 3, and 5%) to 1 ml of culture media and stirring magnetically for 48 h. The ECM solution was centrifuged at 500 g for 10 min to remove any remaining particles. The cold NaOH solution changed the pH of the ECM solution to a range of around 7. This solution was then kept at 4 °C for a week after this stage.

2.4.2. Preparation of hybrid and composite bio-ink

To generate a 6%w/v gelatin (Gel) – 6%w/v sodium alginate (Alg) solution, 0.06 g of gelatin powder was dissolved in 10 ml of DMEM at 40 °C. Then, 0.06 g of alginate was dissolved in gelatin solution, stirred for 1 h, and put into a clean syringe. Three different concentrations of ECM solution (0, 1.5, and 3.5%) were mixed with alginate gelatin solution (6%–6%) to create ECM-Alg-Gel bio-ink. To eliminate trapped air, the samples were centrifuged at 1000 rpm for 1 min [49].

2.4.3. 3D printing of hydrogel scaffolds

3DPL N2 Plus Bioprinter (3DPL, Iran) and CAD/CAM software were used to evaluate the printability. The scaffold dimensions included 7 × 0.15 mm, string spacing 1.3 mm, and string thickness 2 mm. These structures were then saved as STL files and translated to G-code using Replicator G. Using a 21-gauge syringe, bioinks were distributed (21 G, inner diameter 0.51 mm). For printing, the minimum pressure (1.1 bar) and speed of 2 mm/s, and temperature of 25 °C were selected. To preserve the material's integrity over time, glass slides were put in the fridge at 4 °C for 1 h after printing. The printed structures were crosslinked using 300 mM calcium chloride and 0.25% glutaraldehyde for 15 min and then washed for 30 min using DMEM/F12 medium to remove excess calcium ions [36]. The following four groups of scaffolds were printed.

Group 1 (G1): Hybrid scaffolds obtained from the alginate-gelatin solution
Group 2 (G2): Composite scaffolds obtained from alginate-gelatin solution and ECM solution (1.5 wt%)
Group 3 (G3): Composite scaffolds obtained from alginate-gelatin solution and ECM solution (3 wt%)
Group 4 (G4): Composite scaffolds obtained from alginate-gelatin solution and ECM solution (5 wt%)

2.5. Physico-chemical characterizations of placenta ECM-loaded alginate/gelatin 3D print scaffolds

2.5.1. Morphological evaluations

An electron microscope (SEM) was used to assess the final scaffold structure. The samples were first fixed in a solution of 2.5% glutaraldehyde (TAAB, UK) for 2 h and, after washing with PBS, were dehydrated using ascending degrees of alcohols (30%, 50%, 70%, 80%, 90%, and 100%). After lyophilization, the samples were covered with gold, and the scanning electron microscope (EVO ZEISS (Karl Zeiss SMT AG, Oberkochen, Germany) was used to image the samples at an acceleration voltage of 10–20 kV.

2.5.2. Mechanical behaviors

A mechanical testing device (Hct400/25, Zwick/Roell) was used to evaluate modulus and compressive and tensile strength. For this test, samples were prepared with a thickness of 2 mm and a height of 6 mm for all groups. A device (Zwick/Roell, 25/Hct400/25) was subjected to a uniaxial compression test using a load cell of 10 N and a loading speed of 0.1 mm/s. The sample's upper and bottom surfaces were fixed to the compression tester plates to avoid slippage during the tests, and 80% strain was applied to the samples. Also, to evaluate and compare the samples' mechanical strength, the machine stretched the three-dimensional scaffolds at a speed of 0.2 mm/s until rupture. The device recorded the amount of force applied during a pull.

2.5.3. Degradation rate

All scaffolds were weighed before incubating in 2 ml of PBS (pH 7.4) for 30 days at 37 °C, with PBS being changed every three days. The samples were freeze-dried after various times (1 h, 1 day, 7 days, 14 days, and 30 days) and then rinsed with dionized water to eliminate buffer salts. The patients' final weight (Mf) was noted, and the weight reduction percentage was determined using the formula below:

$$\text{Mass loss } (\%) = [(\text{Mf} - \text{Md}) \ / \ \text{Md}] \times 100.$$

2.5.4. Swelling rate

To calculate the swelling of the printed scaffolds, the dry weight of the scaffolds (dry weight Md) was measured and put in 2 ml of PBS (pH 7.4). For 72 h, the scaffolds were incubated at 37 °C. A paper filter was used to remove the unabsorbed PBS at various time intervals of 0.5, 1, 2, 4, 8, 12, 24, 48, and 72 h, and the scaffold weight (Mw) was noted. The following formula was used to determine the scaffold inflation rate:

$$\text{Swelling ratio } (\%) = [(\text{Mw} - \text{Md}) \ / \ \text{Md}] \times 100$$

2.5.5. Fourier transform infrared spectroscopy (FTIR)

FTIR is based on assessing vibrational mutations of molecules and ions of polyaromatic and infrared radiation's absorption to determine the compounds' functional groups. This method determined the organic compounds and functional groups in gelatin-alginate and composite scaffolds. This study used a device (FTIR, SHIMADZU, 8400 S model, Japan) to perform this test. For this purpose, the scaffolds printed were placed by a holder in a spectrometer in the range of 1400 $^{-cm}$ to 14,000^{-cm}.

2.6. In vitro cytobiocompatibility

2.6.1. Cell/scaffold morphology under SEM

A scanning electron microscope (SEM) was used to study the morphology and adhesion of the cells growing on 3D-printed scaffolds. The fibroblast cells were cultured on the construct for 72 h. For SEM micrographs, the samples were fixed with 2.5% glutaraldehyde solution for 2 h at 4 °C. The cells/scaffold constructs were then rinsed with PBS, and dehydrated through graded concentrations of ethanol (50%, 60%, 70%, 80%, 90%, 100% v/v). Finally, the samples were sputtered with gold and examined under an SEM (SEM, AIS2100; Seron Technology, Gyeonggi-do, South Korea) [50].

2.6.2. Cell viability assay

The viability of fibroblast cells cultured on scaffolds was evaluated using 4,5-dimethylthiazol-2-yl-2,5 diphenyl tetrazolium bromide (MTT; Sigma-Aldrich, USA). L929 fibroblast cells (4×10^3) were cultured to allow attachment of the cells in 96 well plates. Then, the different groups of sterilized 3D print scaffolds were added to the cell monolayer for 1, 3 and 7 days. After each prescribed time, the specimens were removed, and the cells were treated with MTT solution for 4 h at 37 °C. After incubation, Dimethyl sulfoxide (DMSO) was used to replace the MTT solution to dissolve formazan crystals that had formed in the mitochondria of living

cells. After 15 min of incubation time, the optical density of the formazan product was read at 570 nm in a microplate reader. The cells with no scaffold served as a control and were considered 100% viability. Triplicate well were performed for each sample [51].

The cell viability percentage was calculated by the following formula (Eq (1)):

$$\text{Cell viability } (\%) = \frac{\text{OD of experiments} - \text{Average OD of negative controls}}{\text{Average OD of positive control}} \times 100 \quad (1)$$

2.7. In vivo biocompatibility

Applying the samples to the skin of NMRI mice showed the biocompatibility of the ECM (5%)-printed scaffolds (weighing 30 g). Following the ethics principles, the scaffolds were first washed for 24 h and sterilized using UV irradiation. Mice were anaesthetized using ketamine and xylazine. Between the second and third lumbar vertebrae, the samples were implanted subcutaneously. The samples were analyzed across two-time intervals: one week (short-term) and four weeks (long-term). After the research period, samples were collected and histologically evaluated using H & E staining. The degree of connective tissue cell penetration into the scaffold was investigated.

2.8. Ex vivo chick embryo CAM assay

An *ex-vivo* CAM assay carried out angiogenesis evaluation of the scaffolds on chick embryos. Locally sourced fertilized eggs were incubated at 37 °C and 60–65% relative humidity. On the third day of incubation, a 21-gauge needle was used to extract 2–3 ml of albumen to generate a space under the eggshell. On day 4, a window of around 1 × 1 cm was gently opened on the wide end of the eggs without damaging the embryo and then sealed with sterile tape. On day 7, the sterilized scaffolds were gently placed on the CAM (as day 0). On day 14, the window was opened (as day 7). The scaffold and areas surrounding the implanted scaffolds were imaged. The images were analyzed using ImageJ software (version 1.8.0_112, Vessel Analysis plugin) to define the relative increased area of the new vessels at day 7 to day 0 of each group using the following formula (Eq (2)):

$$\text{Insease in vessel formation for each groups } (\%) = [(\text{NW7} - \text{NW0}) / \text{NW0}] \times 100 \quad (2)$$

NW0 and NW7 represent new vessel area (mm^2) of each group at day 0 and 7, respectively.

2.9. Animal study

2.9.1. Full-thickness cutaneous wound models

Twenty-seven mice (Male BALB/c, weight 25−30 g) were divided into three groups. After general anaesthesia and complete depilation of the mouse dorsal area, a full-thickness circle wound (about 100 mm^2 in the area) was produced in the upper back region of each mouse. 3D printed Alg/Gel and 5%ECM-Alg/Gel scaffolds were implanted in the wounds. Then, the injuries were wrapped with a plastic mold for protection. At 1, 2, and 3 weeks post-surgery, the implanted site was removed for histological and molecular investigations. The wounds with no implantation were considered as the control group.

2.9.2. In vivo wound healing evaluations

2.9.2.1. Wound closure assessment. Pictures of the wound region were taken on days 0, 7, 14, and 21 following surgery. Image analysis software was used to determine each group's wound area (mm2). The below formula was used to calculate the percent of wound closure (Eq (3)):

$$\text{Percent wound size reduction} = [(A_0 - A_t)/A_0] \times 100 \quad (\text{Eq3})$$

A_0 is the initial wound area (t = 0), and A_t is the wound area at each time point.

2.9.2.2. Histological examination. The collected tissue samples were fixed in 10% formalin, dehydrated through a graded series of ethanol, embedded in paraffin and cut into 6 μm thick slices using a microtome. The slices were stained with H&E, Alcian blue with nuclear fast red and Safranin O with fast green and analyzed under a light microscope (Olympus, Japan). A score protocol from 0 to 4 was used to present each group's wound healing. The lower and higher scores show lower and higher densities of collagen and granulation, respectively.

2.9.2.3. Molecular evaluations of angiogenesis and wound healing. The total RNA was extracted from the tissues using an RNeasy Mini Kit, following the manufacturer's instructions (Cinagen, Tehran, Iran). Gene Runner (version 3.05; Hastings Software Inc, New York, NY, USA) and online primer BLAST (ncbi.nih.gov/tools/primer-blast/) was used to design the primers. The primers used in this study are presented in Table 1. The cDNA was synthesized using a cDNA Archive kit (Applied Biosystems, CA, USA) and random hexamer primers, following the Supplier's instructions. The relative transcript expressions of collagen type I, collagen type III, PDGF, TGF-β1, bFGF, VEGFA, and VEGF-R2 were evaluated by a rotor-gene 6000 real-time PCR (RT-PCR) machine (Corbett Life Science, Sydney, Australia) and an RT-PCR Master Mix (TaKaRa, Dalian, China). The RT-PCR conditions were as follows: 95 °C for 8 min, 45 cycles of 95 °C for 10 s, 60 °C for 25 s, and 72 °C for 25 s. Beta-actin (β-actin) gene was a housekeeping gene for normalizing the expression level. The relative expression fold was calculated using $2^{-\Delta\Delta Ct}$ formula. The tissue collected from the skin with no wounds served as a control.

2.10. Statistical analysis

In the current study, data analysis was undertaken using Prism 7 and SPSS for Windows, version 16.0. (SPSS Inc., Chicago, IL, USA). Variables were provided as the mean ± the standard deviation (SD). An ANOVA followed by a one-way ANOVA, Tukey's post-hoc test, and a repeated-measures ANOVA test was employed for multiple group analyses. In statistical terms, p-values less than 0.05 were considered significant.

3. Results

A schematic of the present research design is illustrated in Fig. 1.

3.1. Efficiency of the decellularization process on placental tissue fragments

ECM bioink preparation consisted of several steps: decellularization, removal of cellular debris from the ECM, and minimization of the ECM damage. The successful elimination of the cells and cells' fragments during the decellularization process was confirmed by H&E and DAPI staining (Supplementary Fig. 1A). The mean cells' nuclei/mm^2 in placenta tissue befor (Ctrl; control) and after (DPS) decellularization process (Supplementary Fig. 1B), as well as the DNA content assay revealed that cell's nuclei and genomic DNA were eliminated from placental tissue after decellularization (Supplementary Fig. 1C).

3.2. Physico-chemical characterizations of placenta ECM-loaded alginate/gelatin 3D print scaffolds

3.2.1. Morphological evaluations

Supplementary Fig. 1D shows the steps of preparing the ECM solution and fabricating the placenta ECM-loaded Alg/Gel 3D print scaffolds. The printed scaffolds showed different surface morphologies under SEM, as shown in Fig. 2. The Alg/Gel scaffolds were identified with flat surfaces.

Table 1
Mouse primers were used in this study for RT-PCR analysis.

	Gene name	Accession number	Sequence	Product size (bp)
1	Beta-actin	NM_007393.5	F: 5′ CTTCTTGGGTATGGAATCCTG R: 5′ GTGTTGGCATAGAGGTCTTTAC	96
2	Collagen I	NM_007742.4	F: 5′ GTTCAGCTTTGTGGACCTC R: 5′ TTGTGGCAGATACAGATCAAG	165
3	Collagen III	NM_009930.2	F: 5′ AAAAGGTGATGCTGGACAG R: 5′ CCACTTTCACCCTTGATACC	177
4	Vascular endothelial growth factor (VEGFA)	NM_001110268.1	F: 5′ TCGCTCCTCCACTTCTGAGG R: 5′ GGCCATTACCAGGCCTCTTC	93
5	Vascular endothelial growth factor receptor-2 (VEGF-R2)	NM_010612.2	F: 5′ AGATGCATTGTGCTGGCTCT R: 5′ AACTCGCCTGTAACCCGACT	122
6	Basic fibroblast growth factor (bFGF)	NM_008006.2	F: 5′ CCGGTCACGGAAATACTCCA R: 5′ CCTTCTGTCCAGGTCCCGTT	89
7	Transforming growth factor-beta 1 (TGF-β1)	NM_011577.2	F: 5′ GGACTACTATGCTAAAGAGGTC R: 5′ GCTTCCCGAATGTCTGAC	126

In contrast, uneven and granular surfaces were seen with increasing ECM concentration. Also, due to a lack of material accumulation and bio-ink homogeneity, printed scaffolds' pore walls seemed like smooth surfaces.

3.2.2. Mechanical behaviors

The stresses and strains of the printed scaffolds were studied, and the results are compared in Tables 2 and 3. Based on the obtained results, the average compressive strength for the samples was reported in the range of 1.24 ± 0.68–0.67 ± 0/31 MPa. The results demonstrated that the compression modulus was increased with the increase of ECM concentration in the scaffolds. There was a significant difference between stress and Young's modulus in the group with 5% ECM and other groups. Additionally, the difference between compressive strength and Young's modulus between 1.5% and 0% was insignificant.

Also, the printed scaffolds' tensile strength was obtained in the range of 0.689 ± 0.65–0.243 - 0.57 MPa. Tensile strength was significantly increased with the increase of ECM content in the scaffolds. The 0% and 5% ECM groups had the lowest and highest mechanical strength, respectively, among the studied groups. The mechanical property results were associated with the micropore size in each scaffold group. The 5% ECM structures showed smaller pores and superior mechanical performance because of the increased connectivity and complex network architecture. The outcomes generally indicated that the mechanical properties of systems containing 5%ECM were more favorable than composite structures.

3.2.3. Degradation rate

Based on the results obtained from the degradation assay, the degradation of the scaffolds increased over time, so that the rate of degradation after 30 days of incubation for Alg/Gel, 1.5%ECM-Alg/Gel, 3%ECM-Alg/Gel and 5%ECM-Alg/Gel were 14.03 ± 2.43, 23.2 ± 0.91,30.16 ± 1.8 and 38.56 ± 2.7, respectively. According to the results, the degradation rate increased with the ECM concentration. So that on days 7, 14, and 30 of incubation, the difference in degradation rate between groups 5%ECM-Alg/Gel (G4) and Alg/Gel (G1) was statistically significant. Nevertheless, there was no noticeable difference between the experimental groups on other incubation days ($P < 0.05$) (Fig. 3 A).

3.2.4. Swelling rate

The ability to absorb liquids is an essential feature of hydrogel scaffolds, associated with the penetration and transport of nutrients, metabolic products, and signaling molecules [36]. The scaffolds' water absorption was assessed by comparing their weights before and after being submerged for different time intervals, until 72 h, in distilled water (Fig. 3B). The findings demonstrated that water absorption increased with the ECM content in the composite scaffolds. The swelling rate (%) at 0.5 h submerged in distilled water in Alg/Gel, 1.5%ECM-Alg/Gel, 3% ECM-Alg/Gel and 5%ECM-Alg/Gel was 116.33% ± 3.12, 120.16% ± 3.45,124.33% ± 4.1 and 136.16% ± 4.8, respectively so that this increase was significant between 5%ECM-Alg/Gel (G4) and Alg/Gel (G1) groups. The swelling ratio increased due to the presence of ECM and the type of solvent (culture medium) used in the hydrogel preparation. The outcomes of this assay were in line with the results of the degradation experiment. Both swelling and degradation results showed a relationship between weight loss and water absorption rate. The swelling rate did not rise considerably in this research until from 0.5 to 72 h following incubation. The equilibrium of the hydrogel scaffolds was attained 30 min after water absorption, while the degradation index did not increase more than 140.70%.

3.2.5. FTIR

The FTIR study findings for gelatin, alginate, and ECM alone, and Alg/Gel, ECM-Alg/Gel contained different ECM contents (0%, 1.5%, 3% and 5%w/v) are shown in Fig. 3C and **D**. The characteristic adsorption bands to the OH tensile frequency were visible at 3392 cm^{-1} on the alginate FTIR diagram. The –COO– group's asymmetric tensile and symmetric tensile vibrations are responsible for the observed peaks at 1617 cm^{-1} and 1417 cm^{-1}, respectively. In addition, the ether group C–*O*-traction C's frequency is associated with the peaks at 1242 cm-1 and 1045 cm-1. The N–H group's tensile vibrations and the OH tensile frequency are connected to a wide band at 3427 cm-1 in gelatin, while the amide's (C = O) tensile vibrations were detected at 1650 cm-1.

Additionally, at wavelengths 1554 and 1452 cm-1, respectively, the N–H flexural and C–N tensile vibrations were demonstrated. The FTIR spectrum obtained from ECM revealed gelatin-like spectra. –OH and –NH tensile vibrations in alginate-gelatin hydrogel scaffolds shifted to 3204 cm-1, representing a partial displacement owing to the strengthening of the hydroxyl bond and the weakening of –NH's intensity. The –COO– group's asymmetric and symmetric tensile vibrations were altered to 1609 cm^{-1} and 1406 cm^{-1}, respectively, and the tensile frequency of the CO group appeared at 1018 cm^{-1}. Gelatin's N–H flexural vibration at 1407 cm^{-1} indicates an intensified amide connection between alginate's carboxylic acid groups and gelatin's amines. In composite scaffolds, the bonds with peaks at 3354 cm^{-1}, corresponding to free hydrogen bonds of the –OH group, and peaks at 3294 cm^{-1}, corresponding to O3S–NH tensile vibrations, were found. In this area, NH-amide tensile vibrations were discovered, showing a link between the amino gelatin molecules and the ECM's carboxylic alginate group and between the amino and carboxylic acid groups. The interaction of the amide groups of these compounds to create hydrogen bonds increases the hydrophilicity of the ECM-hydrogels.

3.3. In vitro cytobiocompatibility

3.3.1. 1. cell-scaffold morphology under SEM

The morphology of L929 fibroblast cells grown for 3 days on the 3D printed scaffolds was observed under SEM (Fig. 4A). As seen, fibroblast cells were attached and spread well to all the 3D scaffolds. The SEM

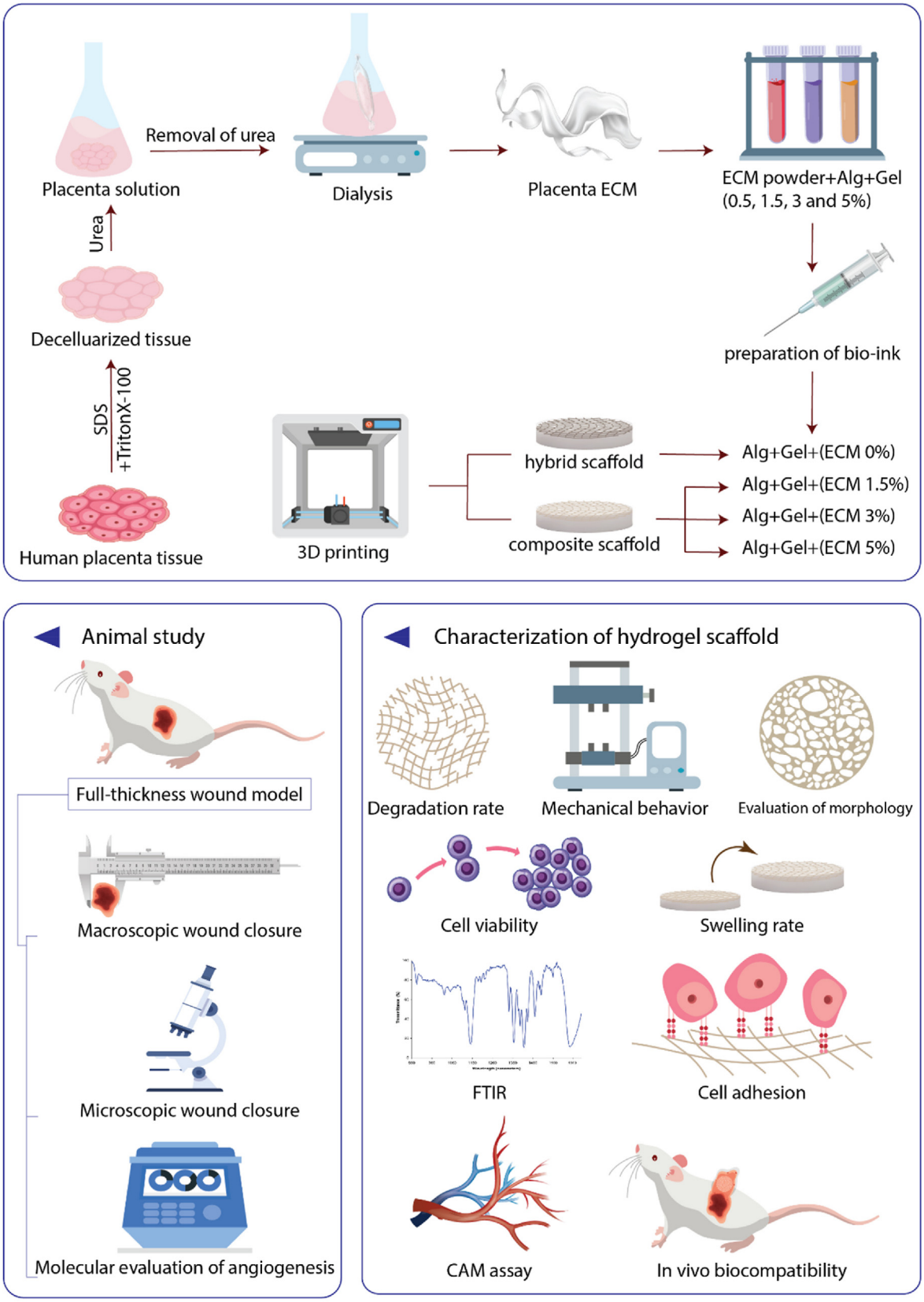

Fig. 1. Summary of the study design: Placental tissue was first decellularized using SDS and Triton-X100, followed by solubilization in urea, dialysis and lyophilization. The placenta ECM solutions with different concentrations (1,5%, 3% and 5%w/v) were printed with alginate and gelatin. Then, the printed scaffolds' physical and biological structure, mechanical behavior, and biocompatibility were investigated. The *in vivo* angiogenesis was determined by CAM assay. The optimized ECM-Alg/Gel 3D printed scaffold was implanted into the full-thickness wound created in mouse mode. The macroscopic, microscopic, and molecular examinations of wound healing were evaluated *in vivo* and compared with those wounds implanted with Alg/Gel and injuries with no treatment (control).

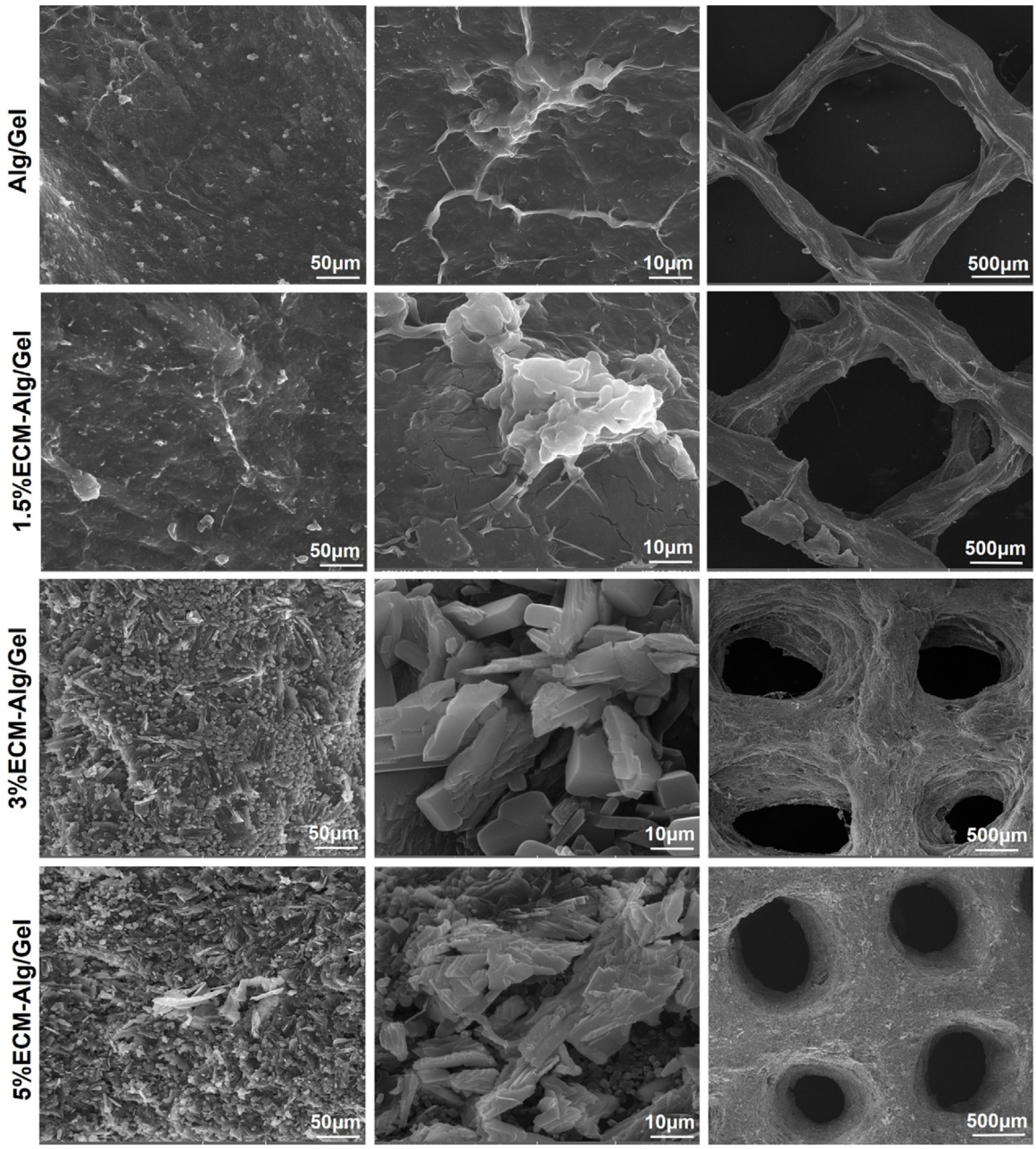

Fig. 2. Morphology and ultrastructure of printed hydrogel scaffolds under SEM. Alg/Gel hybrid scaffolds with flat surfaces and ECM-Alg/Gel composite scaffolds with uneven surfaces and granular states were identified.

Table 2
Characteristics of the compressive strength of printed scaffolds.

Group	Ultimate compressive stress (MPa)	Ultimate compressive strain (%)	Elastic modulus (MPa) (*Young's Modulus)*
0%ECM-Alg/Gel	0.67 ± 0.31	0.61 ± 0.03	0.321 ± 3.62
1.5%ECM-Alg/Gel	0.71 ± 0.45	0.65 ± 0.04	0.398 ± 2.59
3%ECM-Alg/Gel	0.85 ± 0.27	0.76 ± 0.09	0.529 ± 4.43
5%ECM-Alg/Gel	1.24 ± 0.68	0.88 ± 0.07	0.734 ± 5.18

Table 3
Tensile strength properties of printed scaffolds.

Group	Ultimate tensile Stress (MPa)	Maximum tensile strain (%)	Elastic modulus (MPa) (*Young's Modulus)*
0%ECM-Alg/Gel	0.243 ± 0.57	0.35 ± 0.02	0.415 ± 2.63
1.5%ECM-Alg/Gel	0.272 ± 0.42	0.425 ± 0.05	0.493 ± 1.77
3%ECM-Alg/Gel	0.536 ± 0.61	0.67 ± 0.06	1.37 ± 4.26
5%ECM-Alg/Gel	0.689 ± 0.65	1.2 ± 0.08	2.159 ± 4.82

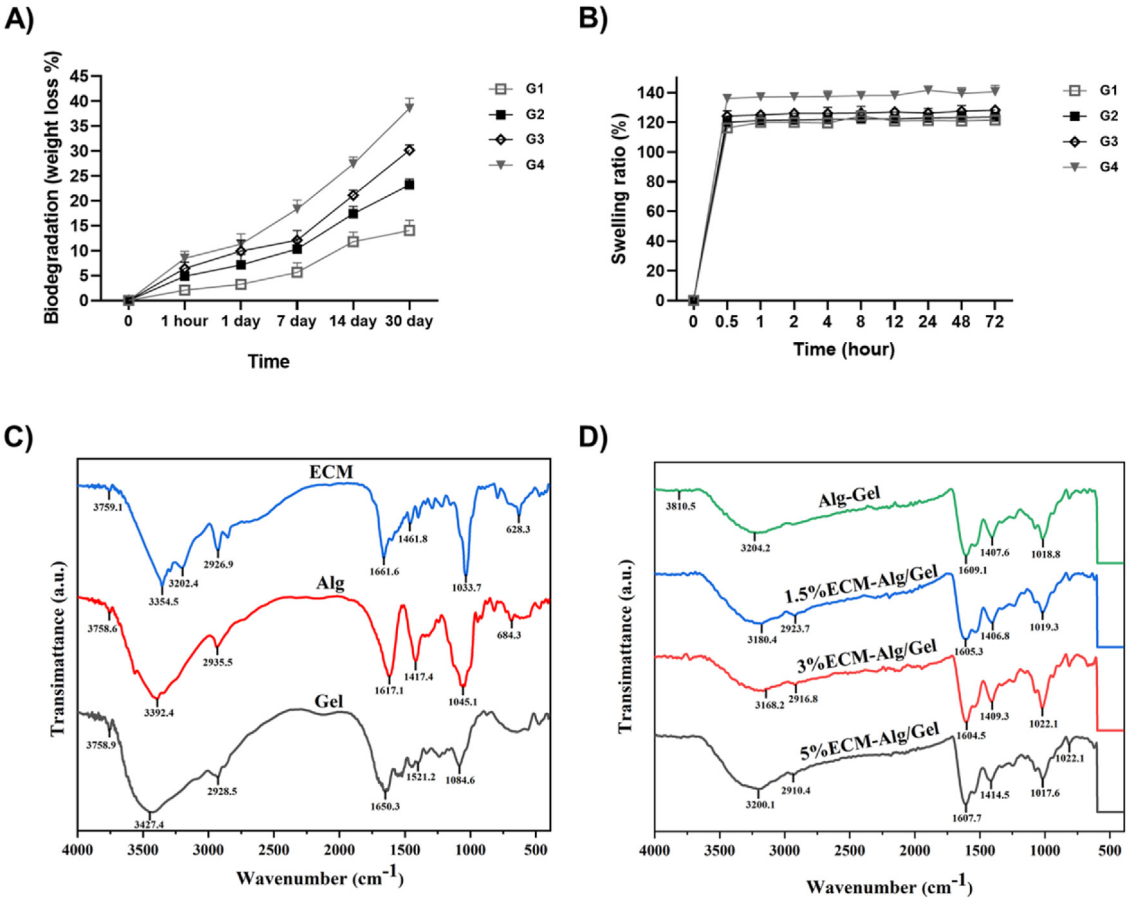

Fig. 3. Degradability, swelling, and FTIR analysis of the printed scaffolds. A) the degradation rate and B) Swelling rate in the printed scaffolds. The data are provided as mean ± SD. G1, G2, G3, and G4 represent Alg/Gel, 1.5%ECM-Alg/Gel, 3%ECM-Alg/Gel and 5%ECM-Alg/Gel, respectively. (*P < 0.05 and **P < 0.01). C) FTIR analyses of ECM, sodium alginate (Alg) and gelatin (Gel). D) FTIR analysis for Alg/Gel alone contained 1.5%, 3% and 5%ECM.

micrographics confirmed good cytocompatibility of the Alg/Gel and ECM-Alg/Gel 3D printed scaffolds.

3.3.2. *Cell viability assay*

The MTT assay indicated that the Alg/Gel 3D printed scaffold and Alg/Gel 3D printed scaffold loaded with ECM (1.5%, 3% and 5% ECM) did not change the viability of the fibroblast cells during 1,3 and 7 days culture periods when compared with control (the cells cultured in cell culture plate as 100% cell viability). Although on day 7, a slight increase in cell viability was observed in those scaffolds with ECM, the difference was insignificant (Fig. 4B).

3.4. *In vivo biocompatibility*

In this investigation, the printed scaffolds were subcutaneously implanted in an animal model, removed after 7 and 28 days post-implantation (Fig. 5A) and stained with H&E. The biodegradation, infiltration of lymphocyte, macrophages, and fibroblasts into the defect site, neovascularization, necrosis and scar formation were evaluated histologically. Microscopic examination of scaffolds after 7 and 28 days of transplantation revealed a normal physiological response. Among the inflammatory cells, the presence of lymphocytes shows an immunological attack on the transplant. A macrophage's presence signifies the breakdown of biological material and the restoration of the injured tissue [52]. Thus, the quantity of inflammatory cells, such as lymphocytes, provides a precise indication of the healing process and the reaction of the local tissue. The examination of biocompatibility by subcutaneous scaffold engraftment revealed the creation of new blood vessels in all samples at days 7 and 28. The results showed that the number of vascular formations was higher in ECM 5%-Alg/gel treated animals than in animals of the Alg/Gel group. Microscopic analysis showed the penetration of connective tissue cells after 7 and 28 days of implantation (Fig. 5B and C), but no signs of inflammation or scar formation were observed. Although the findings demonstrated an increase in the number of lymphocytes in all implants compared with the control sample after 7 and 28 days of implantation, the difference was not significant (P < 0.05). Also, a reduction in macrophage and fibroblast was observed from 7 to 30 days in all groups (Fig. 5D, E, and 5F). The histological analyzes also showed minimal capillaries around the scaffolds, and the attachment of the scaffolds to the adjacent tissue was detectable.

3.5. *CAM assay*

CAM assay was used for angiogenesis evaluation of 3D printed scaffolds. Fig. 6 depicts the scaffolds with ECM that were compared with scaffolds without ECM. After 7 days of incubation, significant growth in the number of blood vessels was detected in the scaffold with ECM compared with the scaffold without ECM. New vessel formation (%) in

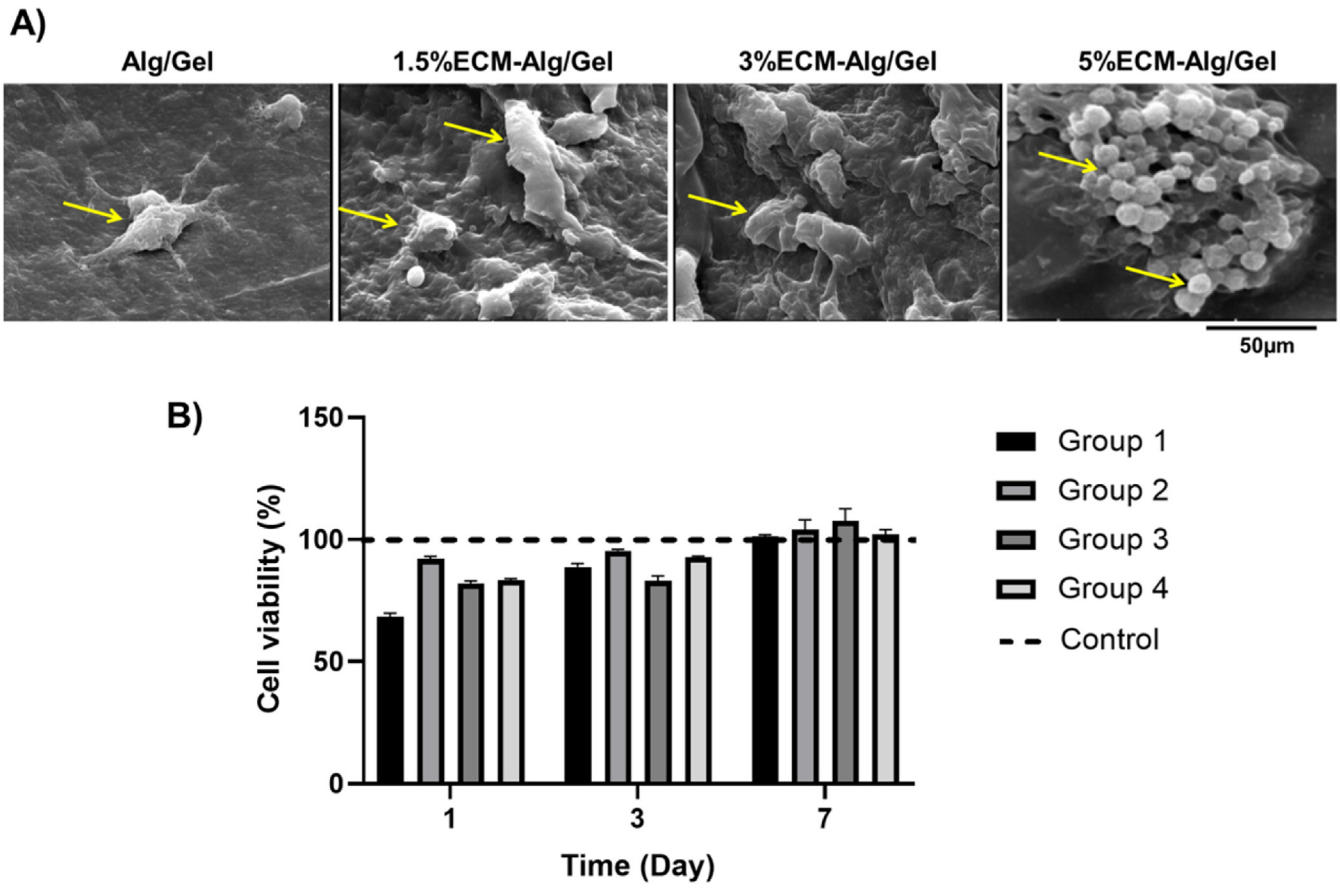

Fig. 4. *In vitro* cytobiocompatibility assays. A) The morphology of fibroblast cells cultured for 3 days on the 3D printed scaffolds under SEM. B) MTT results for fibroblast cells exposed to scaffolds for 1, 3, and 7 days. G1, G2, G3 and G4 represent Alg/Gel, 1.5%ECM-Alg/Gel, 3%ECM-Alg/Gel and 5%ECM-Alg/Gel, respectively. Yellow arrows show the cells.

group 5%ECM-Alg/Gel at day 7 compared with day 0 was around 25% ± 2, while group Alg/Gel showed lower new vessel formation aroun 16.6% ± 2.3.

3.6. Animal study

3.6.1. Macroscopic evaluations

The Alg/Gel and 5%ECM-Alg/Gel 3D printed scaffolds were implanted into full-thickness wounds created in the mouse model. After the treatment of scaffolds for mice excisional injuries, the macroscopic analysis of the wound size, representing wound closure, was carried out. The wound size reduction and wound closure were analyzed at days 0, 7, 14 and 21 days post-surgery. The wounds treated with Alg/Gel and 5% ECM-Alg/Gel scaffolds showed 60.3% and 86.66% wound closure on day 21, respectively. In contrast, injuries without treatment (control group) showed a 55.4% wound size reduction after 21 days. The wounds implanted with Alg/Gel and 5%ECM-Alg/Gel did not show any significant visual signs of infection or inflammation. In injuries without treatment, mild redness was observed as a sign of mild inflammation, especially on day 7 (Fig. 7A).

On day 14 post-implantation, the control group wounds with no treatment and those treated with Alg/Gel scaffolds showed a remarkably slower rate of wound closure (31.2% and 34%, respectively) than those wounds implanted with 5%ECM-Alg/Gel scaffolds (55.3% wound closure rate). A significant difference between the wound size (%) in the 5%ECM-Alg/Gel group and other groups was observed on day 21 (Fig. 7B). The results indicated that the 3D printed ECM-based scaffolds significantly accelerated the re-epithelialization and wound closure compared with other examined groups.

3.6.2. Histological observations

The H&E images of the wounds implanted with Alg/Gel and 5%ECM-Alg/Gel scaffolds at days 7, 14 and 28 post-implantation are presented in Fig. 8A. A thick epidermis with a relative generation of skin appendages was observed in the wounds treated with ECM5%-Alg/Gel. The control wound group (with no treatment) had an irregular and wide epidermal layer with minimum or without the formation of hair follicles (Fig. 8A). According to the histological study, the 5%ECM-Alg/Gel group had a thicker regenerated epithelial layer (filled with keratinocytes) than the Alg/Gel and control groups. H&E stained images revealed almost complete epidermis reconstruction and re-epithelialization in the wounds treated with ECM matrices at day 14 post-implantation. In contrast, the scars in Alg/Gel and control were still open with incomplete re-epithelialization. On day 21, the growth of the epidermis' sublayer, stratum spinosum, was also seen in the 5%ECM-Alg/Gel scaffold-treated group. Compared to other groups, the animals treated with 5%ECM-Alg/Gel 3D printed scaffolds had mature hair follicles. In addition, mature blood vessels in the wounds treated with 5%ECM/Alg/Gel scaffolds were seen compared with control and ECM-Alg/Gel groups (Fig. 8A). Similarly, the wound healing scoring showed that, the 5%ECM/Alg/Gel had higher collagenesis at day 14 and 21 compared with control and Alg/Gel groups. In addition, the wounds treated with Alg/Gel also showed higher collagen density than control at day 21 (Fig. 8B).

In addition, the Safranin O and Alcian blue staining was also carried

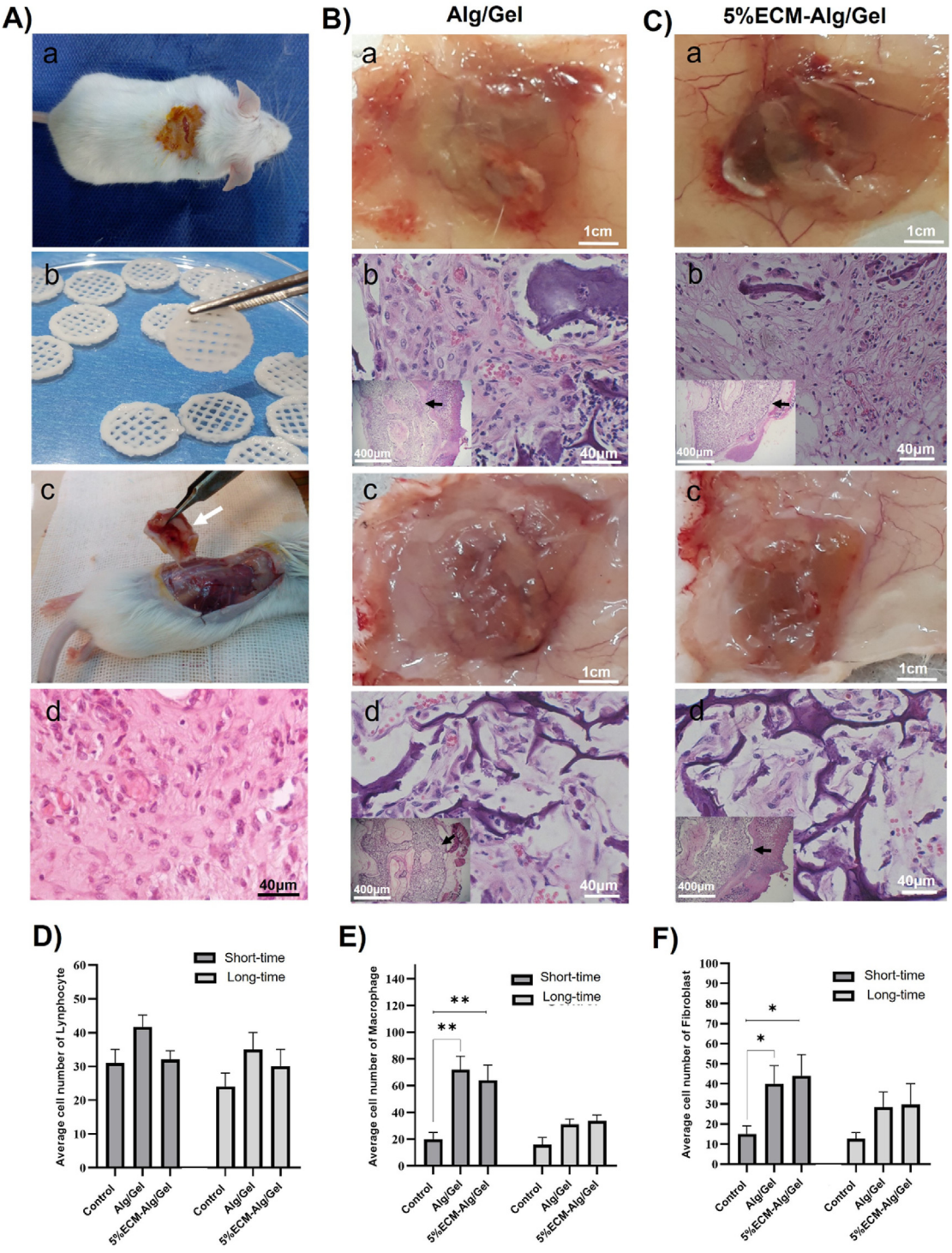

Fig. 5. *In vivo* biocompatibility assessment of printed scaffolds (with and without ECM): **A)** Subcutaneous engraftment of printed scaffolds in NMRI mice (a, b and c). The control group had a left suture snipped with no scaffold inserted (d). **B)** Specimens removed from the skin and stained with H&E after 7 days and short-term (1 week) penetration of cells into the scaffolds (a, b). **C)** Specimens were removed from the skin and stained with H&E after 28 days and long-term (4 weeks) penetration of cells into the scaffolds (c, d). White arrows mark the implanted scaffolds, while a black indicator identifies the scaffolds' link to adjacent tissues. The quantitative examination of mouse connective tissue infiltrating cells, including **D)** lymphocytes, **E)** macrophages, and **F)** fibroblasts inside the scaffolds following long-term (4 weeks) and short-term (1 week) periods of implantation.

out to visualize the tissue morphology with residual biomaterials; the results are shown in Fig. 9A and **B**. The newly formed epidermis and dermis thickness could be seen in each treated and untreated group. Also, the residual biomaterials (indicated with black arrows in Fig. 9) are seen in the Alg/Gel group. A small piece of biomaterial was observed in 5% ECM-Alg/Gel group at day 7 post-treatment.

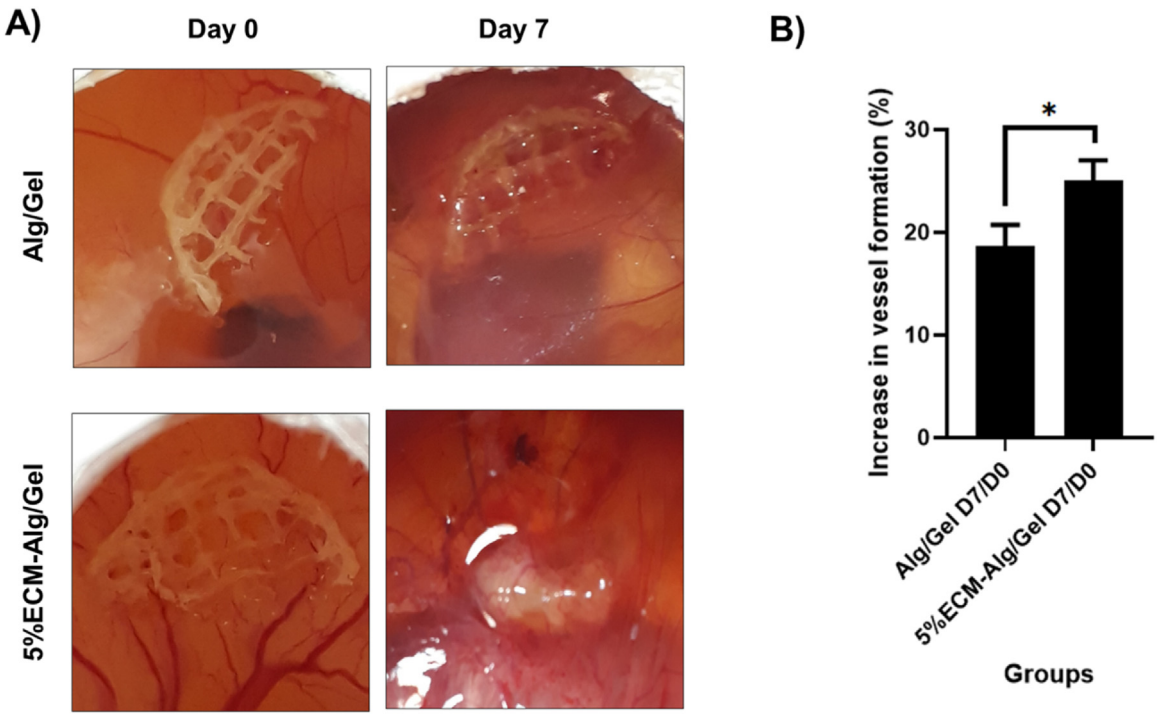

Fig. 6. A) CAM assay results for the angiogenesis potential of the scaffolds with and without ECM. B) Increase in new vessel formation (%) in each group on day 7 compared with day 0. * indicates $p < 0.05$.

3.6.3. Molecular evaluations of angiogenesis and wound healing

The evaluation of wound healing and angiogenesis in the wounds treated with Alg/Gel and 5%ECM-Alg/Gel 3D printed scaffolds in gene expression level was carried out by RT-PCR technique, and the relative gene expression fold was measured and compared with those in control (no treatment) wounds (gene expression fold was considered as 1). The RT-PCR results are shown in Fig. 10. At all the sacrificed time points, the expression of the examined wound healing genes (TGFβ1, Col1a and Col3a) and pro-angiogenic genes (bFGF, VEGFA and VEGFR) in the wounds treated with Alg/Gel and 5%ECM-Alg/Gel was considerably more than control wounds with no treatment. The presence of 5%ECM in the 3D printed scaffolds dramatically induced the expression of TGFβ1, Col1a and Col3a compared with Alg/Gel with no ECM. Alg/Gel and 5% ECM-Alg/Gel showed no significant difference in Col1a gene expression on days 14 and 21 and Col3a on days 21.5%ECM-Alg/Gel showed a significantly highest level of bFGF, VEGFA and VEGFR gene expression compared with other experimental groups in all time points.

4. Discussion

Wound healing is a complex biological process limited to deep wounds, and tissue regeneration may not occur naturally and completely. Due to the limitations of the autologous skin graft method, including pain and complications of the patient donor area and source limitation, other methods, such as reconstructive medicine, have been introduced. Scaffolds can improve skin function and repair deep wounds by creating an appropriate environment for cell growth, proliferation and differentiation. They can also create a barrier against infection and external damage [53–56]. A variety of advanced therapeutic approaches, from different biomaterials to cell-derived matrices to deliver stem cells, have been used for wound healing and skin regeneration [57]. Skin scaffolds have been used in various fibrous, sponge, hydrogel, 3D print or composite forms [58–60]. In recent decades, ECM-derived scaffolds have been developed as skin substitutes from multiple tissue sources of the dermis, amniotic/chorionic tissues, intestines, and peritoneum [61,62]. The scaffolds based on natural ECM modulate angiogenesis, cell migration, and cellular organization during wound healing due to the preservation of the 3D structure, cell attachment, and availability of biologically active components [63–65].

Various methods are commonly used for tissue decellularization based on chemical, physical, and biological agents [66,67]. Recently, we achieved a successful decellularization approach of placental tissue. We have subsequently, with great success, used them for sponges for skin and bone tissue regeneration, as well as in several reproductive applications [14,68,69]. This study used the same procedure to decellularize placental tissue with minor modifications. Histological and DNA content assays were carried out to verify that the cells were successfully removed after decellularization. Similar to this study, Willemse et al. (2020) also used SDS alone or in combination with Triton to decellularise pig liver. According to their report, Triton + SDS gave less damage to collagen and GAGs compared to tissues treated with SDS alone [70]. The findings of our research also demonstrated that SDS removed nuclear debris.

As a result, the decellularization of human placental tissue fragments using the SDS/Triton protocol effectively eliminated cell debris and preserved ECM compounds of placental tissue fragments. In addition to the decellularization protocol, an appropriate digestive solution can also affect the quality of ECM-derived hydrogels. Most studies use pepsin (an enzyme purified from pig gastric juice) with hydrochloric acid or acetic acid to prepare ECM-derived hydrogels. Previous studies have reported that the use of acid, due to its high acidity, can irreversibly disintegrate intermolecular bonds of collagen and jeopardize the polymerization of filaments during future gelatinization [71]. Enzyme solubilization also alters ECM-derived hydrogel proteins. Interestingly Pouliot et al. (2016) examined the ECM protein profile of lung tissue before and after enzymatic digestion using SDS-PAGE,. In the protein profile, spots of small proteins were observed in the solution after enzymatic digestion, indicating that small proteins were degraded by the enzyme [72]. In another study by Marc et al. (2015) urea was employed for extracting ECM from human placental tissue and downstream solubilization processes. Their procedure preserved the ECM proteins, cytokines and growth factors at physiological levels [73]. In our study, on the other hand, non-covalent bonds were further disrupted due to the usage of urea and increased

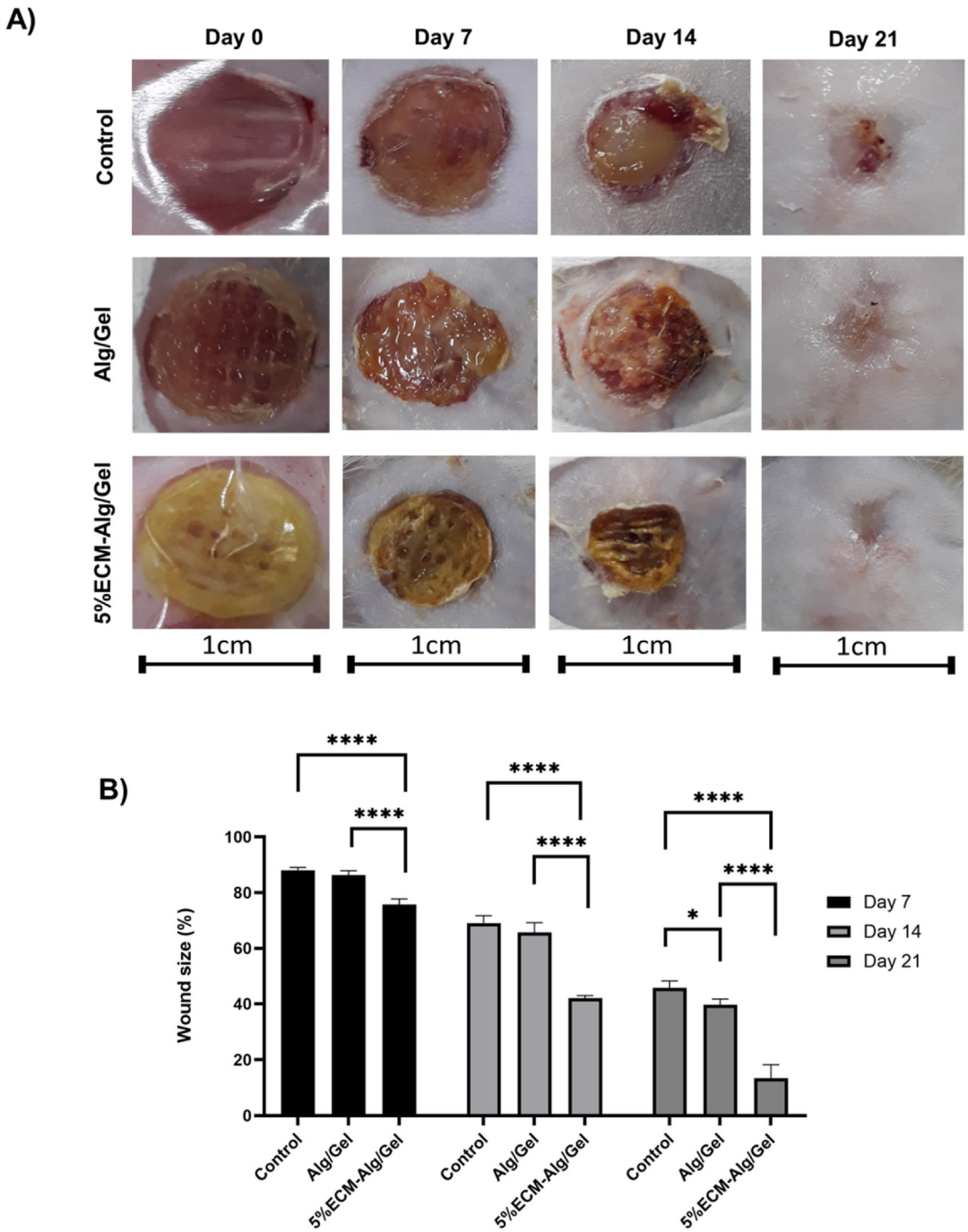

Fig. 7. A) Macroscopic images of the wound size after treatment with Alg/Gel and 5%ECM-Alg/Gel 3D printed scaffolds for three weeks. Scale bars represent 1 cm. **B)** The wound size reduction (%) at days 7, 14 and 21 post-treatment. $P < 0.0001$, $P < 0.001$, $P < 0.01$, and $P \leq 0.05$ are indicated by ****, ***, **, and *, respectively.

solubility of ECM proteins, which confirmed the results of other studies [36].

In this study, we used sodium alginate/gelatin as a supporting material to increase the mechanical properties of placental tissue ECM. For this purpose, different sodium alginate/gelatin concentrations were tested to make a hydrogel solution with the highest printability capacity. Low concentrations of sodium alginate/gelatin mixture did not lead to hydrogel formation due to low viscosity, and high concentrations of gel mixture did not allow extrusion. But finally, the sodium alginate/gelatin hybrid with 6%/6%w/v ratio was optimized as a printable hydrogel. In the present study, different concentrations of human placental ECM (1.5%, 3% and 5%) were also composited with sodium alginate/gelatin hybrid to prepare a printable bio-ink. One of our challenges in this study was the crosslinking of ECM-based printed hydrogel. $CaCl_2$, glutaraldehyde, and culture media were used to improve ECM's printability and mechanical characteristics. The different concentrations of $CaCl_2$ and glutaraldehyde were used at other times for crosslinking. Finally, a concentration of 300 mM $CaCl_2$ with 0.25% glutaraldehyde and duration of 30 min were selected, which limits the speed of scaffold decomposition and cell viability was not impaired. Then, morphological, structural, mechanical, biocompatibility and cell viability characteristics of the 3D-printed hydrogel scaffolds were investigated.

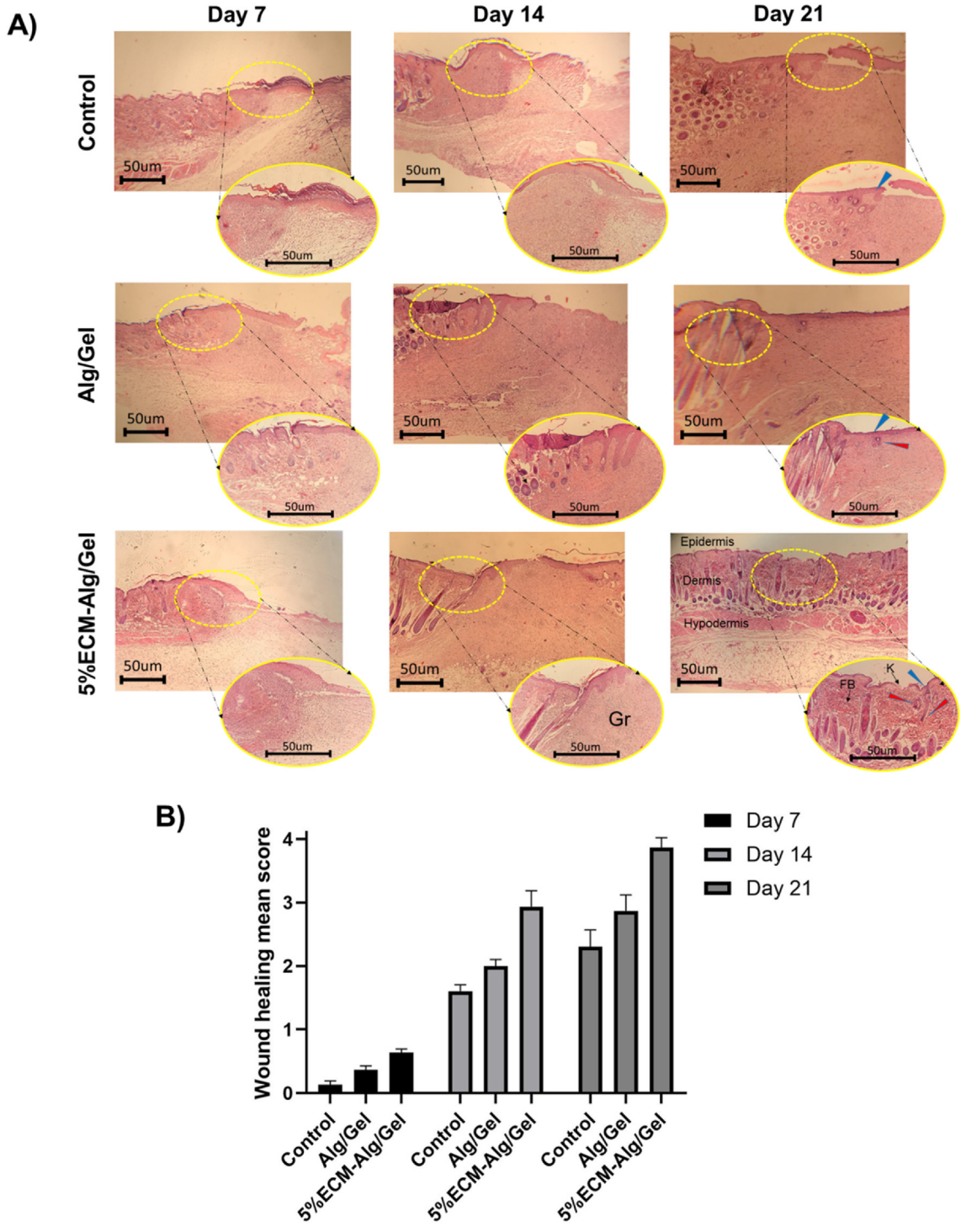

Fig. 8. Histological analysis of wound tissue. A) H&E histological staining of the full-thickness wounds with no treatment (control), treated with Alg/Gel and 5% ECM/Alg/Gel 3D printed scaffolds. On days 7, 14 and 21 post-surgery. Blue arrows represent the regenerated epidermal layer. Red arrow: hair follicles, K: Keratinocytes, FB: Fibroblasts and Gr: Granulation tissue. **B)**. Scoring of the wound healing after treatment with 3D biomaterials and no treated wounds.

3D printing makes it possible to fabricate scaffolds with controlled and more precise structures compared to salt-leaching [74], foaming [75], electro-spinning [34], freeze-drying [76] techniques, and do not have the problem of repeatability and uncontrolled geometry [77]. Many natural and synthetic biomaterials have been used as bio-ink for 3D printing applications [78]. Notably, a bio-ink must be biocompatible for cell growth, mechanically stable, and have high fidelity after printing [40,79,80]. After the introduction of 3D bioprinting, the search for printable and biocompatible polymers has become more and more essential. According to the report, the use of 3D bioprinting for wound healing and skin regeneration began in 2012 with collagen bio-inks. Natural biopolymers have different advantages over synthetic biopolymers due to their high similarity to human ECM, and therefore lack the same properties in terms of promoting cell differentiation, spreading

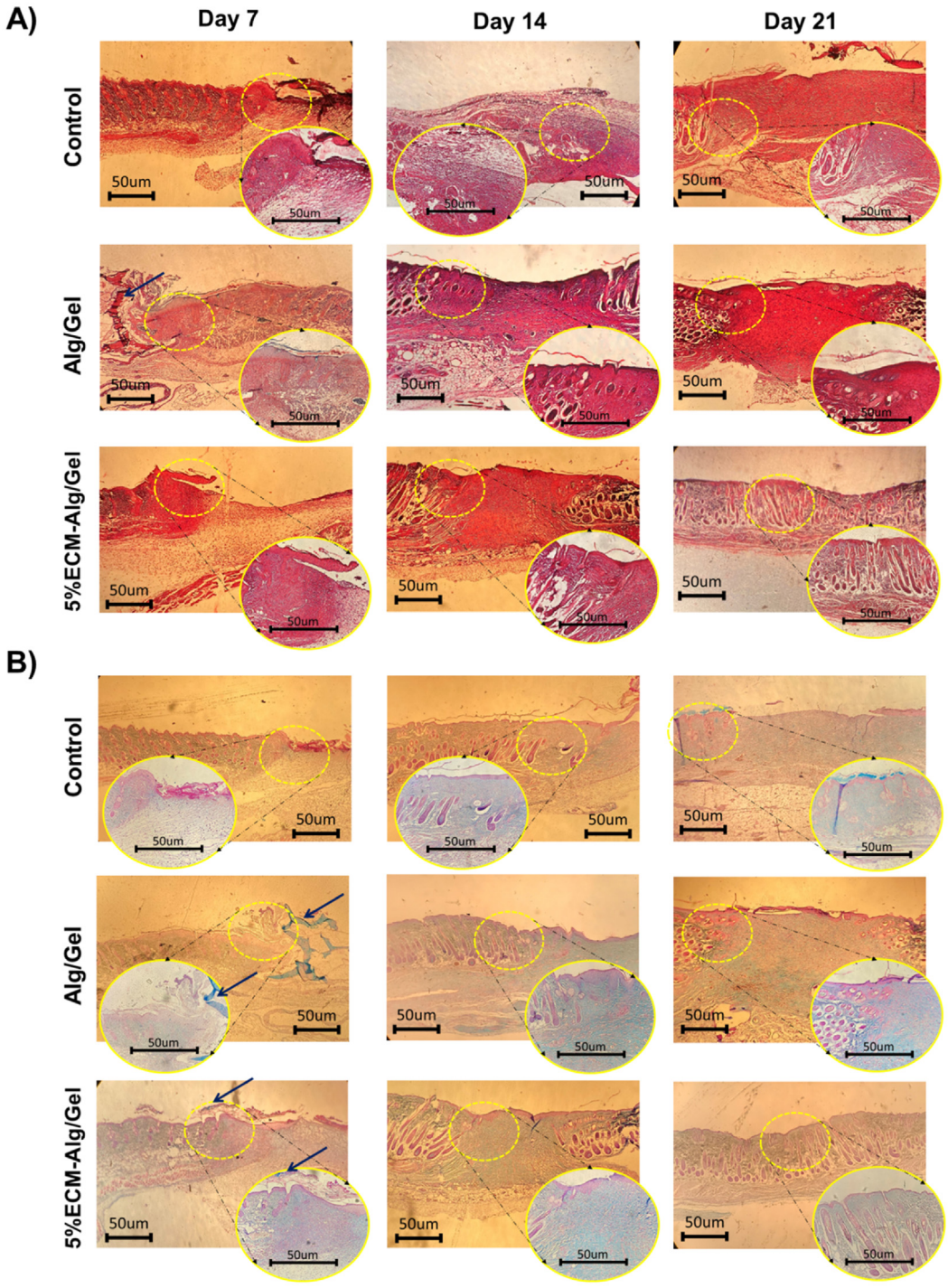

Fig. 9. Safranin O with fast green and Alcian blue with nuclear fast red histological analysis. **A)** Safranin and **B)** Alcian blue staining of the full-thickness wounds with no treatment (control), treated with Alg/Gel and 5%ECM/Alg/Gel 3D printed scaffolds, at days 7, 14 and 21 post-surgery. The residual biomaterials are indicated with black arrows.

and proliferation [81,82]. For this reason we have used human placenta ECM-based printed scaffolds. Indeed, Decellularized ECM-based bio-inks are an intriguing choice for 3D printing of tissues and organs due to their unique biochemical features. Fabrication of ECM-derived bio-ink for 3D printing is challenging. Nevertheless, their structural stability after printing is insufficient because of poor mechanical properties of decellularized ECM-based bio-inks. In recent years, advances have been made to improve the printability of decellularized ECM-based bio-inks to create structures diplaying similar mechanical properties as natural tissues. For instance, some studies have used supporting materials such as PCL [83], PEVA [84] or Pluronic F-127 [85] to build 3D models. Decellularized ECM-based bio-inks and cross-linkable hydrogels can also be employed to create stable mechanical structures without supporting materials. Cross-linkable hydrogels significantly increase the mechanical properties of printed designs. For example, a study combined decellularized ECM solution obtained from liver tissue with HA-Gel. The resulting compound

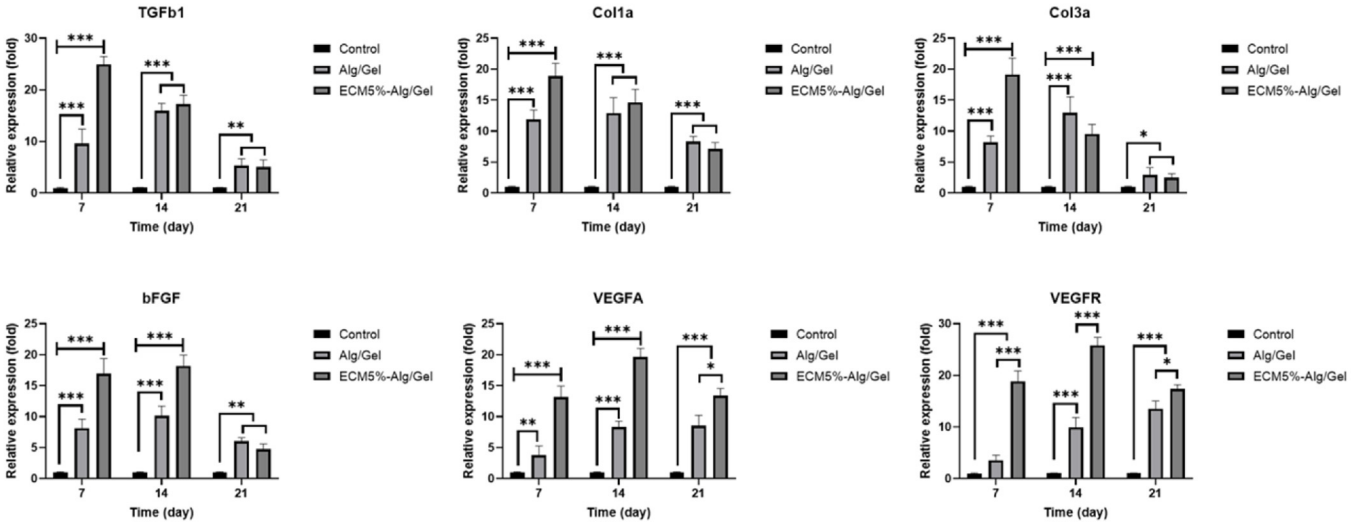

Fig. 10. Relative gene expression (fold) in the wound with no treatment (control) and treated with Alg/Gel and 5%ECM-Alg/Gel for wound healing genes (TGFβ1, Col1a and Col3a) and pro-angiogenic genes (bFGF, VEGFA and VEGFR). *, ** and *** indicate the significant difference with $p \leq 0.05$, $p < 0.01$, and $p < 0.001$, respectively.

was crosslinked by a thiol-acrylate bond, which provided a soft, extrudable gel [86]. In another study, decellularized ECM obtained from vascular tissue was composited with alginate through an ionic cross-linking procedure. This bio-ink was printed with CPF127 solution to allow the alginate gelation by releasing Ca^{+2} ions [87]. Recently, we investigated the effect of different concentrations of testicular tissue ECM (0, 1.5%, 3% and 5%) to fabricate printed hydrogel scaffolds. We found that the combination of crosslinker $CaCl_2$, glutaraldehyde and a culture medium as a solvent could stabilize the structure, while simultanously increasing the viability of seeded cells [36].

It is well-documented that a humid environment leads to faster and more effective wound healing, improves metabolism in the wound and reduces bacterial pain, infection, and scar formation [88]. Therefore, an ideal skin scaffold should absorb wound secretions and moisten the damage. For this reason, scaffold swelling behavior facilitates cell migration, proliferation, oxygen uptake, and waste disposal [89]. The swelling property of hydrogel scaffolds depends on hydrophilic groups that absorb water and transport nutrients. Our results showed that increased ECM concentration increased the swelling rate of the resulting scaffolds. This increase may be attributable to the presence of hydrophilic groups, such as amines, hydroxyl, and carboxyl, which was confirmed by Rezaei et al. They reported that the decellularized testis ECM-derived scaffold had the highest water uptake in the first 30 min, and no significant difference in water uptake was observed until 72 h later. They also reported that the swelling rate increased with increasing testis ECM scaffold density [90]. Our study followed the highest amount of water absorption in scaffolds containing 5% ECM.

The effect of different concentrations of ECM on the mechanical properties of our printed scaffolds was also investigated in this study. Our findings indicated that increasing the ECM concentration increased compressive and tensile strength (0.734 ± 5.18 and 2.159 ± 4.82, respectively). The increase in stress and Young's modulus in systems containing ECM could be due to new hydrogel bonds (between the amide groups) confirmed by Xing et al. [91].

The degradation rate of a scaffold should be proportionate to its hydrogel composition type and the rate of tissue regeneration. The skin scaffold should not be destroyed before the wound healing stage is complete. Therefore, in this study, the degradation rate of samples during 30 consecutive days was investigated. In our research, with increasing the incubation time, the percentage of scaffold degradation increased slowly. The scaffold degradation rate decreased over time and was lower in the second week than the first one. The scaffold weight remained approximately 61.44% intact after 30 days of incubation, and scaffolds containing 5% ECM showed the maximum degradation rate. In general, the degradation rate of specimens seems appropriate for skin tissue engineering, as they do not entirely disintegrate within three weeks [88].

FTIR spectroscopy results gave us insight into the integration of ECM with Alg/Gel compounds and the preservation of the molecular structure of scaffolds after crosslinking. Our findings demonstrated that the reproducibility to fabricate scaffolds is high, and there is no excess or impurity peak in the scaffold's composition. Tissue engineering scaffolds must have suitable surface chemical properties and non-cytotoxicity so that after cell culture, proper adhesion and attachment are established between the cells and the scaffold. SEM imaging was used to evaluate morphology and cell adhesion after seeding cells on the scaffold. It is noteworthy that with the increase in ECM concentration, some granules were observed on the samples' surface, thus providing suitable connection points for cell expansion.

The excellent cell binding properties of the printed scaffolds can be attributed to the structure's hydrophilicity and unique ECM properties. It seems that the cells were in shock after first day of culturing on the scaffolds. Still, by increasing the incubation time to 3 and 7 days, the survival rate increased due to the adaptation and proliferation of fibroblast cells. The results of MTT test showed that scaffolds containing ECM were not toxic for fibroblast cells and provided an effective substrate for wound healing during 7 days of culturing time. The high survival rate and cell adhesion in all scaffolds in our study indicated the proper performance of hydrogel scaffolds [92].

In addition to mechanical stability, biocompatibility is a vital feature of any scaffold that should be evaluated *in vivo* [93]. In this regard, a subcutaneously implanted mouse model was used to assess the *in vivo* biocompatibility of ECM-based printed scaffolds. Scaffolds were subcutaneously implanted for 7 and 28 days and then the samples were histologically stained to determine the cell penetration into the scaffolds and host immune system reaction. Cell penetration is an essential feature of scaffolds because it proves that scaffolds have the potential for cell infiltration, growth and migration and that fibroblasts can begin their cellular function after penetration. The results of the histological analysis

confirmed that the printed scaffolds showed high compatibility. There were also no signs of severe inflammation, long-term external reaction, or wound formation. Quantitatively, there was a slight increase in the average number of cells within the scaffold, but this difference was not statistically significant. The results of our study were consistent with the data of other studies that have examined the biocompatibility of testis ECM-based printed scaffolds after subcutaneous transplantation and showed no signs of scar formation. Also, Dulany et al. (2020) showed that porous nanocomposite scaffolds containing poly (1,8 octanediol-*co*-citrate), beta-tricalcium phosphate and cerium oxide nanoparticles were biocompatible after subcutaneous transplantation in mice and supported cell penetration and had a minimal immune response surrounding the scaffolds [94]. According to the results of biological and biomechanical tests, the 5% ECM-Alg/Gel composite scaffold was considered an optimal scaffold and examined for further angiogenic and *in vivo* wound healing investigations. CAM analysis was carried out to assess the impact of placental ECM loaded in Alg/Gel printed scaffold on the angiogenesis capacity *in vivo*. The results showed that the percentage of blood vessels in samples containing ECM was significantly higher than in scaffolds without ECM. , The angiogenic property of decellularized placental sponge was proved in our recently published study, as it could keep its angiogenesis potential even after six months' preservation at −20 °C [68].

A human placental ECM (hp-bioink)-derived bioink was developed by Duan et al. in 2022 with good printability and bioactivity. In suspended hydrogels, they were able to embed and print 1%–2% of the hp-bioink. They demonstrated how hp-bioink facilitated angiogenesis *in vivo* and correleated this with human umbilical vein endothelial cell assembly *in vitro* [49]. In another study, Ji-Yeun Park (2011) examined the effect of human placenta injection on mouse wounds. They injected the human placenta sample into the mice's back area and investigated the wound healing process on days 7, 14, and 15. Their results showed that the human placenta potentially affected skin wound healing by regulating the entire wound-healing process, including inflammation, proliferation, and reconstruction [95]. Clinical studies by Brigido et al. (2017), in a similar v vein, shown that the matrix of human tissue without cellularity could cause wound healing through cellular migration, rapid tissue regeneration, and functional tissue remodeling [96]. It was also shown that decellularized placental sheets effectively promoted keratinocyte and epithelial cell migration and neovascularization, consequently enhancing the quality of wound healing [97].

In the present study, the wound closure was significantly faster in the group treated with 5%ECM-Alg/Gel than in those wounds treated with ECM-free scaffolds and no treatment groups. The components of the base membrane and the active biological molecules in the placenta ECM can play a valuable role in the production of the primary membrane with the proper structure, the growth and distinction of keratinocytes, and the normalization of epithelial architecture. Throughout the recovery period, wound healing using ECM-based scaffolds was significantly superior to those without ECM. The ECM samples were well merged into the host tissue due to cell penetration within 7 days. In the wound implanted with the ECM scaffold, keratinocytes migrated rapidly into the wound site, and new epithelial cells developed at the wound's edges. Notably, the injuries implanted with 5%ECM-Alg/Gel scaffolds were quickly reconstructed between 7 and 14 days. A continuous epidermis completely covered the damage implanted with 5%ECM-Alg/Gel. The epidermal appendages were entirely formed on day 14 and rebuilt on 28th. Safranin O with fast green and Alcial Blue with nuclear fast red staining was performed to determine the tissue morphology with residual biomaterials in the wound bed. The residual biomaterials were only observed at day 7 post-surgery of both Alg/Gel, and 5%ECM-Alg/Gel treated wounds. The residual biomaterials are seen in the Alg/Gel group, while a small piece of biomaterial was observed in 5%ECM-Alg/Gel group at day 7 post-treatment. This finding indicates that the presence of 5%ECM in Alg/Gel construct accelerated the *in vivo* degradation rate, which is consistent with our *in vitro* biodegradation (weight loss %) data. Some growth factors, like bFGF, inhibit the phenotypic transformation of fibroblasts into myofibroblasts, which may be implicated in wound contraction. Regenerating injuries are complicated, including inflammation, neovascularization, forming new tissue, and regeneration of damaged tissue. Neovascularization supports low oxygen levels in regenerated tissues [98]. In line with our study, Kim et al. (2018) used a decellularized skin ECM solution to produce a 3D model of human skin with total thickness. The ECM loaded with human skin fibroblast was printed as a dermis structure. After the thermal crosslinking of the printing structure, the epidermal compounds were printed with the distribution of the culture medium containing the keratinocytes using the inkjet module. The exact design was also printed using collagen inkjet as a control group. In the ECM structures, better epidermal organization and ECM secretion were observed. Also, the printed structures improved the efficiency of wound healing compared with the control group [99]. The placenta contains several angiogenesis factors such as IGF-1, VEGFA, HGF, PDGF-B, bFGF and others [100], and can enhance neovascularization and wound healing. This tissue is considered an excellent candidate for skin tissue engineering applications. Our study observed significant neovascularization ability and accelerated re-epithelialization in the ECM-loaded scaffolds compared with other experimental groups. The wounds treated with the ECM scaffold showed increased expression of wound-healing genes and pro-angiogenic genes such as bFGF, VEGFA, and VEGFR. Inflammatory cell-derived factors contribute to neovascularization by encouraging the formation of new capillaries and stimulating endothelial cell proliferation. On the 7th day, fewer small veins were observed in the wound implanted with the ECM scaffold compared to the ECM-free and control groups. Our results revealed the potential of a 5%ECM-Alg/Gel 3D printed scaffold with improved biomedical and biological properties, angiogenesis, and wound healing capacity compared to Alg/Gel.

5. Conclusion

Bioprinting is an emerging approach for reconstructing a cellular microenvironment similar to that of the native ECM. This makes them, in turn, suitable candidates for skin tissue engineering. In this research, human placenta ECM solutions composed of different ECM components and endogenous growth factors were 3D printed. By increasing the concentration of ECM, the structural, mechanical, and cell interaction properties were improved. In addition, ECM-based printed hydrogels showed the ability to promote angiogenesis *in vivo*. Our findings showed that ECM-based printed hydrogels might significantly enhance neovascularization and wound healing and are thus a great scaffolding candidate for skin tissue engineering. By simulating the complexity of the natural extracellular matrix, our research can provide a new opportunity to print vascular tissues and organs.

Credit author statement

MG and MZ conceived and designed the study. ZB, MRF, HGH, DJ, SA and MNB performed the experiments. ZB, MG, ZN, SA and DJ analyzed the data and interpreted the results. ZB, HGH, DJ and SA prepared the manuscript. MG, GO, RLR, SCK, GO and ADP reviewed during the manuscript preparation and revised the manuscript.

Ethics approval statement

This investigation was conducted following the Helsinki guidelines for animal care and surgery. The Institutional Animal Care and Ethical Committee of Bushehr University of Medical Sciences approved the study's ethics and protocols for animal study and human placental tissue collection.

Patient consent statement

Not applicable.

Declaration of competing interest

The authors declare that they have no known competing financial interests or personal relationships that could have appeared to influence the work reported in this paper.

Data availability

Data will be made available on request.

Acknowledgements

The authors acknowledge 3DPL Company (Tehran, Iran) for cooperating during this investigation. This research was supported by funding from the Bushehr University of Medical Sciences (IR.BPUMS.REC.1400.183). GO acknowledges the support of the Spanish Ministry of Economy, Industry, and Competitiveness (PID2019-106094RB-I00/AEI/10.13039/501100011033).

Appendix A. Supplementary data

Supplementary data to this article can be found online at https://doi.org/10.1016/j.mtbio.2023.100666.

References

[1] B.L. Dearman, S.T. Boyce, J.E. Greenwood, Frontiers in Surgery (2021) 362.
[2] G. Sun, J. Qin, F. Chen, P. Wu, Front. Bioeng. Biotechnol. (2022) 244.
[3] L.-P. Kamolz, P. Kotzbeck, M. Schintler, S. Spendel, Eur. Surg. (2022) 1–7.
[4] Á. Sierra-Sánchez, K.H. Kim, G. Blasco-Morente, S. Arias-Santiago, NPJ Regenerative Medicine 6 (1) (2021) 1–23.
[5] H. Sorg, D.J. Tilkorn, J. Hauser, A. Ring, Bioengineering 9 (7) (2022) 298.
[6] S. Tavakoli, M.A. Kisiel, T. Biedermann, A.S. Klar, Biomedicines 10 (1) (2022) 118.
[7] Y. Shimizu, E.H. Ntege, H. Sunami, Regenerative Therapy 21 (2022) 73–80.
[8] Z. Azari, S. Nazarnezhad, T.J. Webster, S.J. Hoseini, P. Brouki Milan, F. Baino, S. Kargozar, Wound Repair Regen. 30 (4) (2022) 421–435.
[9] Y. Guo, J. Huang, Y. Fang, H. Huang, J. Wu, Chem. Eng. J. (2022), 134690.
[10] R. Ni, C. Luo, H. Ci, D. Sun, R. An, Z. Wang, J. Yang, Y. Li, J. J. M. T. B. Sun, 18 (2023), 100539.
[11] A.D. Widgerow, Ann. Plast. Surg. 73 (2) (2014) 239–244.
[12] A. Yazdanpanah, Z. Madjd, M. Pezeshki-Modaress, Z. Khosrowpour, P. Farshi, L. Eini, J. Kiani, M. Seifi, S.C. Kundu, R. Ghods, Artif. Organs 46 (6) (2022) 1040–1054.
[13] P. Ramhormozi, J. Mohajer Ansari, S. Simorgh, M. Nobakht, J. Burn Care Res. 41 (5) (2020) 1069–1078.
[14] Z. Khosrowpour, S.M. Hashemi, S. Mohammadi-Yeganeh, M. Moghtadaei, P. Brouki Milan, L. Moroni, S.C. Kundu, M. Gholipourmalekabadi, Artificial Organs, 2022.
[15] P. Zare, M. Pezeshki-Modaress, S.M. Davachi, H. Chahsetareh, S. Simorgh, N. Asgari, M.A. Haramshahi, R. Alizadeh, Z. Bagher, M. Farhadi, J. Biomed. Mater. Res. 110 (6) (2022) 1199–1209.
[16] S.V. Murphy, A. Atala, Nat. Biotechnol. 32 (8) (2014) 773–785.
[17] S.H. Tan, Z.H. Ngo, D. Leavesley, K. Liang, Tissue Eng. B Rev. 28 (1) (2022) 160–181.
[18] S.Y. Nam, S.-H. Park, Biomimetic Medical Materials (2018) 335–353.
[19] W.C. Wilson Jr., T. Boland, Anat. Rec. Part A: discoveries in molecular, cellular, and evolutionary biology 272 (2) (2003) 491–496.
[20] R. Oklu, Y.S. Zhang, K. Yue, J. Aleman, K. Mollazadeh-Moghaddam, S.M. Bakht, J. Yang, W. Jia, V. Dell'Erba, P. Assawes, Ann Biomed Eng 45 (1) (2016) 148–163.
[21] F. Liu, X. Wang, Polymers 12 (8) (2020) 1765.
[22] S. Balasubramanian, M.-E. Aubin-Tam, A.S. Meyer, 3D Printing for the Fabrication of Biofilm-Based Functional Living Materials, ACS Publications, 2019, pp. 1564–1567.
[23] Z. Bashiri, M. Gholipourmalekabadi, R. Falak, I. Amiri, H. Asgari, N.P.S. Chauhan, M. Koruji, Int. J. Biol. Macromol. 217 (2022) 824–841.
[24] I. Bianchi, A. Forcellese, S. Gentili, L. Greco, M. Simoncini, Procedia CIRP 105 (2022) 380–385.
[25] P. Rupert, J. Wound Care 25 (Sup4) (2016) S17–S21.
[26] V.A.S. David, V.R. Güiza-Argüello, M.L. Arango-Rodríguez, C.L. Sossa, S.M. Becerra-Bayona, Front. Bioeng. Biotechnol. (2022) 10.
[27] L. Flynn, J.L. Semple, K.A. Woodhouse, The Japanese society for biomaterials, and the Australian society for biomaterials and the Korean society for biomaterials, J. Biomed. Mater. Res. Part A: An Official Journal of The Society for Biomaterials 79 (2) (2006) 359–369.
[28] K.H. Schneider, P. Aigner, W. Holnthoner, X. Monforte, S. Nürnberger, D. Rünzler, H. Redl, A.H. Teuschl, Acta Biomater. 29 (2016) 125–134.
[29] M.J. Smith, S.G. Dempsey, R.W. Veale, C.G. Duston-Fursman, C.A. Rayner, C. Javanapong, D. Gerneke, S.G. Dowling, B.A. Bosque, T. Karnik, J. Biomater. Appl. 36 (6) (2022) 996.
[30] J.P. Alves-Lopes, J.-B. Stukenborg, Hum. Reprod. Update 24 (2) (2018) 176–191.
[31] R.-H. Fu, Y.-C. Wang, S.-P. Liu, T.-R. Shih, H.-L. Lin, Y.-M. Chen, J.-H. Sung, C.-H. Lu, J.-R. Wei, Z.-W. Wang, Cell Transplant. 23 (4–5) (2014) 621–630.
[32] M. Gholipourmalekabadi, B. Farhadihosseinabadi, M. Faraji, M.R. Nourani, Burns 46 (6) (2020) 1254–1271.
[33] F. Pati, J. Jang, D.-H. Ha, S. Won Kim, J.-W. Rhie, J.-H. Shim, D.-H. Kim, D.-W. Cho, Nat. Commun. 5 (1) (2014) 1–11.
[34] Z. Bashiri, M. Zahiri, H. Allahyari, B. Esmaeilzade, Andrologia (2022), e14380.
[35] S. Simorgh, P.B. Milan, M. Saadatmand, Z. Bagher, M. Gholipourmalekabadi, R. Alizadeh, A. Hivechi, Z. Arabpour, M. Hamidi, C. Delattre, Materials 14 (14) (2021) 3909.
[36] Z. Bashiri, I. Amiri, M. Gholipourmalekabadi, R. Falak, H. Asgari, C.B. Maki, A. Moghaddaszadeh, M. Koruji, Biomater. Sci. 9 (9) (2021) 3465–3484.
[37] S. Lee, H.S. Lee, J.J. Chung, S.H. Kim, J.W. Park, K. Lee, Y. Jung, Int. J. Mol. Sci. 22 (6) (2021) 2886.
[38] D.O. Visscher, H. Lee, P.P. van Zuijlen, M.N. Helder, A. Atala, J.J. Yoo, S.J. Lee, Acta Biomater. 121 (2021) 193–203.
[39] M. Qasim, F. Haq, M.-H. Kang, J.-H. Kim, Int. J. Nanomed. 14 (2019) 1311.
[40] J. Gopinathan, I. Noh, Biomater. Res. 22 (1) (2018) 1–15.
[41] M. Gómez-Guillén, B. Giménez, M.a. López-Caballero, M. Montero, Food Hydrocolloids 25 (8) (2011) 1813–1827.
[42] J. Lee, D. Kim, C.H. Jang, G.H. Kim, Theranostics 12 (9) (2022) 4051.
[43] R.S. Barreto, P. Romagnolli, P. Fratini, A.M. Mess, M.A. Miglino, J. Tissue Eng. 10 (2019), 2041731419867962.
[44] D.E. Wildman, Placenta 32 (2011) S142–S145.
[45] S.E. Lobo, L.C.P. Leonel, C.M. Miranda, T.M. Coelho, G.A. Ferreira, A. Mess, M.S. Abrão, M.A. Miglino, Cells Tissues Organs 201 (4) (2016) 239–252.
[46] F. Asgari, S. Khosravimelal, M. Koruji, Z. A. Ahovan, A. Shirani, A. Hashemi, H. G. Hamidabadi, N. P. S. Chauhan, L. Moroni, R. L. J. M. S. Reis, and E. C, 2021, 121, 111814..
[47] F. Asgari, H.R. Asgari, M. Najafi, B.S. Eftekhari, M. Vardiani, M. Gholipourmalekabadi, M. J. J. o. M. S. M. i. M. Koruji 32 (5) (2021) 47.
[48] A. Azadbakht, S. Alizadeh, Z. Aliakbar Ahovan, Z. Khosrowpour, M. Majidi, S. Pakzad, S. Shojaei, N.P.S. Chauhan, M. Jafari, M.J.M.B. Gholipourmalekabadi, Macromol. Biosci. 23 (2) (2023), 2200386.
[49] Y. Duan, W. Huang, B. Zhan, Y. Li, X. Xu, K. Li, X. Li, X. Liu, S. Ding, S. Wang, Biomed. Mater. 17 (5) (2022), 055009.
[50] Z.A. Ahovan, S. Khosravimelal, B.S. Eftekhari, S. Mehrabi, A. Hashemi, S. Eftekhari, P.B. Milan, M. Mobaraki, A.M. Seifalian, M. Gholipourmalekabadi, Int. J. Biol. Macromol. 164 (2020) 4475–4486.
[51] S. Simorgh, Z. Bagher, M. Farhadi, S.K. Kamrava, M.E. Boroujeni, Z. Namjoo, F.Q. Hour, S. Moradi, R.J.M.N. Alizadeh, Mol. Neurobiol. 58 (2021) 3835–3847.
[52] Z. Xia, J.T. Triffitt, Biomed. Mater. 1 (1) (2006) R1.
[53] S. Huang, X. Fu, J. Contr. Release 142 (2) (2010) 149–159.
[54] T. Agarwal, R. Narayan, S. Maji, S. Behera, S. Kulanthaivel, T.K. Maiti, I. Banerjee, K. Pal, S. Giri, Int. J. Biol. Macromol. 93 (2016) 1499–1506.
[55] P. Ramhormozi, J.M. Ansari, S. Simorgh, H.R. Asgari, M. Najafi, M. Barati, A. Babakhani, M. J. A. o. A.-A. A. Nobakht 236 (2021), 151652.
[56] S. Alizadeh, P. Farshi, N. Farahmandian, Z.A. Ahovan, A. Hashemi, M. Majidi, A. Azadbakht, M. Darestanifarahani, K.S. Sepehr, S. C. J. I. J. o. B. M. Kundu 229 (2023) 22–34.
[57] R. Hazrati, S. Davaran, Y. Omidi, Reactive and Functional Polymers, 2022, 105233.
[58] P. Agrawal, S. Soni, G. Mittal, A. Bhatnagar, Int. J. Low. Extrem. Wounds 13 (3) (2014) 180–190.
[59] I. Sukmana, J. Artif. Organs 15 (3) (2012) 215–224.
[60] P. Farshi, R. Salarian, M. Rabiee, S. Alizadeh, M. Gholipourmalekabadi, S. Ahmadi, N.J.P.E. Rabiee, Science 62 (9) (2022) 2741–2749.
[61] M. Dussoyer, A. Michopoulou, P. Rousselle, Appl. Sci. 10 (10) (2020) 3435.
[62] M. Gholipourmalekabadi, S. Khosravimelal, Z. Nokhbedehghan, M. Sameni, V. Jajarmi, A.M. Urbanska, H. Mirzaei, M. Salimi, N.P.S. Chauhan, M. Mobaraki, ACS Biomater. Sci. Eng. 5 (3) (2019) 1487–1496.
[63] A. Eweida, M. Marei, BioMed Res. Int. 2015 (2015).
[64] A. Joshi, S. Choudhury, S.B. Gugulothu, S.S. Visweswariah, K. Chatterjee, Biomacromolecules 23 (7) (2022) 2730–2751.
[65] P.K. Parameshwar, L. Sagrillo-Fagundes, N.A. Portilho, W. Pastor, C. Vaillancourt, C. Moraes, Reproductive Toxicology, 2022.
[66] P.M. Crapo, T.W. Gilbert, S.F. Badylak, Biomaterials 32 (12) (2011) 3233–3243.
[67] A. Neishabouri, A.S. Khaboushan, F. Daghigh, A.-M. Kajbafzadeh, M.M. Zolbin, Front. Bioeng. Biotechnol. (2022) 10.
[68] F. Asgari, S. Khosravimelal, M. Koruji, Z.A. Ahovan, A. Shirani, A. Hashemi, H.G. Hamidabadi, N.P.S. Chauhan, L. Moroni, R.L. Reis, Mater. Sci. Eng. C 121 (2021), 111814.
[69] R. Sajed, A. H. Zarnani, Z. Madjd, S. Arefi, M. R. Bolouri, S. Vafaei, A. Samadikuchaksaraei, M. Gholipourmalekabadi, N. Haghighipour, and R. J. A. O. Ghods, 2022, 46(3), 375-386..
[70] J. Willemse, M.M. Verstegen, A. Vermeulen, I.J. Schurink, H.P. Roest, L.J. van der Laan, J. de Jonge, Mater. Sci. Eng. C 108 (2020), 110200.

[71] G.E. Wnek, G.L. Bowlin, Encyclopedia of Biomaterials and Biomedical Engineering, CRC Press, 2008.
[72] R.A. Pouliot, P.A. Link, N.S. Mikhaiel, M.B. Schneck, M.S. Valentine, F.J. Kamga Gninzeko, J.A. Herbert, M. Sakagami, R.L. Heise, J. Biomed. Mater. Res. 104 (8) (2016) 1922–1935.
[73] M.C. Moore, V. Pandolfi, P.S. McFetridge, Biomaterials 49 (2015) 37–46.
[74] L.N. Woodard, K.T. Kmetz, A.A. Roth, V.M. Page, M.A. Grunlan, Biomacromolecules 18 (12) (2017) 4075–4083.
[75] O. Mahony, O. Tsigkou, C. Ionescu, C. Minelli, L. Ling, R. Hanly, M.E. Smith, M.M. Stevens, J.R. Jones, Adv. Funct. Mater. 20 (22) (2010) 3835–3845.
[76] L.S. Connell, F. Romer, M. Suárez, E.M. Valliant, Z. Zhang, P.D. Lee, M.E. Smith, J.V. Hanna, J.R. Jones, J. Mater. Chem. B 2 (6) (2014) 668–680.
[77] J.J. Chung, H. Im, S.H. Kim, J.W. Park, Y. Jung, Front. Bioeng. Biotechnol. (2020) 1251.
[78] F.E. Montero, R.A. Rezende, J.V. Da Silva, M.A. Sabino, Front. Mech. Eng. 56 (2019).
[79] A. Panwar, L.P. Tan, Molecules 21 (6) (2016) 685.
[80] Z. Xia, S. Jin, K. Ye, SLAS TECHNOLOGY: Translating Life Sciences Innovation 23 (4) (2018) 301–314.
[81] L. Valot, J. Martinez, A. Mehdi, G. Subra, Chem. Soc. Rev. 48 (15) (2019) 4049–4086.
[82] J.E. Kim, S.H. Kim, Y. Jung, Tissue engineering and regenerative medicine 13 (6) (2016) 636–646.
[83] F. Pati, D.-H. Ha, J. Jang, H.H. Han, J.-W. Rhie, D.-W. Cho, Biomaterials 62 (2015) 164–175.
[84] S. Das, S.-W. Kim, Y.-J. Choi, S. Lee, S.-H. Lee, J.-S. Kong, H.-J. Park, D.-W. Cho, J. Jang, Acta Biomater. 95 (2019) 188–200.
[85] P.L. Lewis, M. Yan, J. Su, R.N. Shah, Acta Biomater. 85 (2019) 84–93.
[86] A. Skardal, M. Devarasetty, H.-W. Kang, I. Mead, C. Bishop, T. Shupe, S.J. Lee, J. Jackson, J. Yoo, S. Soker, Acta Biomater. 25 (2015) 24–34.
[87] G. Gao, J.H. Lee, J. Jang, D.H. Lee, J.S. Kong, B.S. Kim, Y.J. Choi, W.B. Jang, Y.J. Hong, S.M. Kwon, Adv. Funct. Mater. 27 (33) (2017), 1700798.
[88] Y.D. Nokoorani, A. Shamloo, M. Bahadoran, H. Moravvej, Sci. Rep. 11 (1) (2021) 1–20.
[89] Q.L. Loh, C. Choong, Tissue Eng Part B Rev 19 (6) (2013) 485–502.
[90] T.R. Topraggaleh, M.R. Valojerdi, L. Montazeri, H. Baharvand, Biomater. Sci. 7 (4) (2019) 1422–1436.
[91] Q. Xing, K. Yates, C. Vogt, Z. Qian, M.C. Frost, F. Zhao, Sci. Rep. 4 (1) (2014) 1–10.
[92] Y. Yang, Q. Lin, C. Zhou, Q. Li, Z. Li, Z. Cao, J. Liang, H. Li, J. Mei, Q. Zhang, Front. Cell Dev. Biol. 8 (2020) 250.
[93] S. Wu, X. Liu, K.W. Yeung, C. Liu, X. Yang, Mater. Sci. Eng. R Rep. 80 (2014) 1–36.
[94] K. Dulany, K. Hepburn, A. Goins, J.B. Allen, J. Biomed. Mater. Res. 108 (2) (2020) 301–315.
[95] J.-Y. Park, J. Lee, M. Jeong, S. Min, S.-Y. Kim, H. Lee, Y. Lim, H.-J. Park, Nutr. Res. Prac. 8 (4) (2014) 404–409.
[96] S.A. Brigido, S.C. Carrington, N.M. Protzman, Clin. Podiatr. Med. Surg. 35 (1) (2018) 95–104.
[97] J.S. Choi, J.D. Kim, H.S. Yoon, Y.W. Cho, Tissue Eng. 19 (3–4) (2013) 329–339.
[98] S.A. Eming, T. Krieg, J.M. Davidson, J. Invest. Dermatol. 127 (3) (2007) 514–525.
[99] B.S. Kim, Y.W. Kwon, J.-S. Kong, G.T. Park, G. Gao, W. Han, M.-B. Kim, H. Lee, J.H. Kim, D.-W. Cho, Biomaterials 168 (2018) 38–53.
[100] B.E. Uygun, A. Soto-Gutierrez, H. Yagi, M.-L. Izamis, M.A. Guzzardi, C. Shulman, J. Milwid, N. Kobayashi, A. Tilles, F. Berthiaume, Nat. Med. 16 (7) (2010) 814–820.